

MIMO UV NLOS Communications

---

A Thesis

Presented to  
the faculty of the School of Engineering and Applied Science  
University of Virginia

---

in partial fulfillment  
of the requirements for the degree

Master of Science

by

Ankit Gupta

May

2012

APPROVAL SHEET

The thesis  
is submitted in partial fulfillment of the requirements  
for the degree of  
Master of Science

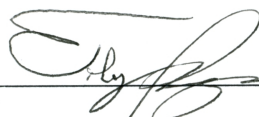


AUTHOR

The thesis has been read and approved by the examining committee:



Advisor



Accepted for the School of Engineering and Applied Science:



Dean, School of Engineering and Applied Science

May  
2012

## Acknowledgments

I would like to thank all these people who have made this thesis possible and because of whom my graduate experience has been one that I will cherish forever.

I would like to express my sincere gratitude to my advisor Prof. Maite Brandt-Pearce for her continuous guidance during my study and research. She is a source of constant encouragement and inspiration and I thank her for believing in me. I could not have imagined having a better mentor for my graduate study.

Prof. Stephen Wilson's insightful feedback at different stages of my research was thought-provoking and helped me work better. His perspective and guidance was extremely valuable, and necessary, for this research.

Prof. Toby Berger, Prof. Ben Calhoun and Prof. Ronald Williams have my appreciation for the best courses I have taken during my education. These courses equipped me with the technical know-how to perform my research.

This research would not have been possible without the financial support provided by the National Science Foundation (NSF) grant number ECCS-0901682.

Finally, I would like to thank my parents for their love and support throughout this research.

## Abstract

Rich atmospheric scattering in the ultraviolet (UV) wavelength enables non-line-of-sight (NLOS) communications, providing new opportunities for communications. With recent advances in UV sources and detectors, NLOS UV communications have received increasing interest for diverse applications. This thesis studies corresponding NLOS UV channels and multiple-input multiple-output (MIMO) systems.

The author considers propagation and channel modeling in the context of NLOS deep UV ( $<300$  nm) communications. Based on NLOS communication link geometry and UV signal interaction with the atmosphere, a computationally flexible numerical integration approach is presented that can be used to generate the UV scattering channel impulse response and path loss for noncoplanar geometries. The UV NLOS link is studied for various transmitter and receiver elevation angles, separation distances and path losses. The numerical integration approach developed compares favorably with published results, and lays the foundation to efficiently model the UV NLOS MIMO system.

Since UV NLOS communications rely on directed communications, the research explores sectoring the scattering atmosphere into non-overlapping volumes defined by the transmit/receive angles and using this as a multiplex-

ing technique to provide higher gain and interference rejection. For low data rates, the UV NLOS channel can be modeled as a nondispersive channel. Symbol by symbol detectors are developed and compared for this case. The author also investigates the effects of channel delay spread on communication quality, i.e., studying data rate limitation from the induced intersymbol interference from dispersive channels. Receiver structures are developed for a simple 2X2 MIMO case, based on the dispersive model for the UV NLOS scattering channel.

The channel models and receiver structures are used to study performance of a NLOS UV system for a number transceiver structures and data rate, range and system configuration constraints. Spatial multiplexing relaxes pointing constraints for UV NLOS systems by allowing 3dB gains in path loss for misdirected transmitter-receiver pairs. It also improves receiver performance significantly by reducing ISI. These investigations and results provide valuable guidance for NLOS UV communication system design in a real environment.

# Contents

<b>List of Figures</b>	<b>iv</b>
<b>Acronyms</b>	<b>x</b>
<b>1 Introduction</b>	<b>1</b>
1.1 UV NLOS Communications . . . . .	2
1.2 Motivation . . . . .	5
1.3 Literature Review . . . . .	9
1.4 Thesis Outline . . . . .	13
<b>2 Ultraviolet NLOS Channel Modeling and Loss Analysis</b>	<b>15</b>
2.1 Numerical Integration Approach for Link Loss . . . . .	17
2.2 Numerical Integration Approach for Impulse Response Calcula- tion . . . . .	22
2.3 Shadowing Effects Due to Obstacles . . . . .	23
2.4 Numerical Results . . . . .	25

2.5	Computational Complexity . . . . .	34
2.6	Chapter Summary . . . . .	35
<b>3</b>	<b>Receiver Design for Nondispersive Channels</b>	<b>37</b>
3.1	Channel Path Loss Model Description . . . . .	38
3.2	Receiver Description and Noise Model . . . . .	40
3.3	MIMO Model . . . . .	42
3.4	Receiver Design . . . . .	46
3.4.1	Decision Algorithm for the SISO Case . . . . .	48
3.4.2	Decoder Design for 2X2 MIMO Case Using a Decision Threshold . . . . .	50
3.4.3	Zero forcing/Decorrelation Receiver . . . . .	52
3.4.4	MMSE Receiver . . . . .	54
3.4.5	One Shot ML Receiver . . . . .	56
3.5	Numerical Results . . . . .	59
3.6	Chapter Summary . . . . .	64
<b>4</b>	<b>Receiver Design for ISI Case</b>	<b>66</b>
4.1	ISI Model of the Channel . . . . .	68
4.2	Communication System and Impulse Response Coefficient De- scription . . . . .	71
4.3	MAP Receiver Design . . . . .	75

4.4	MLSE Receiver Design . . . . .	78
4.5	Numerical Results . . . . .	84
4.6	Chapter Summary . . . . .	94
<b>5</b>	<b>Conclusion</b>	<b>96</b>



# List of Figures

2.1	Geometry of the NLOS UV link. . . . .	18
2.2	Shadowing due to obstacles in a NLOS UV link geometry. Figure modified and taken from [51]. . . . .	24
2.3	Impulse response for $\theta_1 = 90^\circ$ , $\theta_2 = 45^\circ$ , $\phi_1 = 17^\circ$ , $\phi_2 = 30^\circ$ , and $d = 100$ m using Reilly's approach [27] and the numerical integration method. Numerical integration is plotted for both uniform and Gaussian transmitted beams, and also for a case including shadowing. . . . .	26
2.4	Impulse response for $\theta_1 = 20^\circ$ , $\theta_2 = 30^\circ$ , $\phi_1 = 17^\circ$ , $\phi_2 = 30^\circ$ , and $d = 100$ m using Reilly's approach [27] and the numerical integration method. Numerical integration is plotted for both uniform and Gaussian transmitted beams. . . . .	28
2.5	Path loss vs. range for $\theta_1 = 80^\circ$ , $\theta_2 = 60^\circ$ , $\phi_1 = 10^\circ$ and $\phi_2 = 30^\circ$ , using different methods. . . . .	29

2.6	Path loss vs. range for $\theta_1 = 20^\circ$ , $\theta_2 = 30^\circ$ , $\phi_1 = 17^\circ$ and $\phi_2 = 30^\circ$ , using different methods. . . . .	30
2.7	Path loss vs. the range for $\theta_1 = 40^\circ$ , $\theta_2 = 20^\circ$ , $\phi_1 = 17^\circ$ and $\phi_2 = 30^\circ$ , using different methods. . . . .	31
2.8	Path loss vs. transmitter to receiver azimuth skew for different geometries. . . . .	32
2.9	Path loss vs. transmitter to receiver azimuth skew for spatial multiplexing case. . . . .	32
2.10	Top view of a spatially multiplexed system with two narrower transmitter beams instead of a larger beam. . . . .	33
3.1	UV NLOS MIMO system. Figure taken from [49] and modified.	42
3.2	UV NLOS 2X2 MIMO system. . . . .	44
3.3	UV communication principle diagram. . . . .	46
3.4	Probability of detection and false alarm. . . . .	49
3.5	BER performance for $h_{11} = -99.65$ dB, $h_{12} = 0$ , $h_{21} = 0$ and $h_{22} = -96.81$ dB. Simulated probability of error vs transmit- ted power is plotted for all three receivers and the analytical result from (3.18). . . . .	60

3.6	BER performance for $h_{11} = -99.65$ dB, $h_{12} = -102.66$ dB, $h_{21} = -102.66$ dB and $h_{22} = -96.81$ dB. Simulated prob- ability of error vs transmitted power is plotted for all three receivers: ZF, MMSE and ML. . . . .	61
3.7	Ideal constellation corresponding to the NLOS UV link with no interference. . . . .	63
3.8	Constellation corresponding to the NLOS UV link with severe interference. . . . .	64
4.1	(a) State diagram of the channel $h = (1, 0.5)$ for binary trans- mission. (b) One stage of the corresponding two-state trellis. .	70
4.2	Impulse response for UV NLOS communication link with $\theta_1 =$ $85^\circ$ , $\theta_2 = 85^\circ$ , $\phi_1 = 40^\circ$ , $\phi_2 = 90^\circ$ and $d = 20$ m. . . . .	73
4.3	Eye pattern for a UV NLOS communication link with $\theta_1 =$ $85^\circ$ , $\theta_2 = 85^\circ$ , $\phi_1 = 40^\circ$ , $\phi_2 = 90^\circ$ and $d = 20$ m operating at 3 Mbps. . . . .	74
4.4	Impulse response coefficients for channel with memory 2. . . .	75
4.5	A sample trellis. . . . .	80
4.6	Example of progression of the Viterbi algorithm through the trellis. . . . .	81

4.7	Trellis diagram for the 2 tap channel model of the 2X2 MIMO system. . . . .	82
4.8	Trellis diagram for the 3 tap channel model of the 2X2 MIMO system. . . . .	83
4.9	Receiver performance comparison for system operating at 3 Mbps and with geometry $\theta_1 = 85^\circ$ , $\theta_2 = 85^\circ$ , $\phi_1 = 40^\circ$ , $\phi_2 = 90^\circ$ and $d = 20$ m for both the transmitter-receiver pairs. Channel with a memory of 2 symbols. . . . .	84
4.10	Receiver performance comparison for system operating at 3 Mbps and with no interference between channels. The system geometry is $\theta_1 = 85^\circ$ , $\theta_2 = 85^\circ$ , $\phi_1 = 40^\circ$ , $\phi_2 = 90^\circ$ and $d = 20$ m for both the transmitter-receiver pairs. Channel with a memory of 2 symbols. . . . .	85
4.11	Receiver performance comparison for system operating at 2 Mbps and with geometry $\theta_1 = 85^\circ$ , $\theta_2 = 85^\circ$ , $\phi_1 = 40^\circ$ , $\phi_2 = 90^\circ$ and $d = 20$ m for both the transmitter-receiver pairs. Channel with a memory of 1 symbol. . . . .	86

4.12	MLSE receiver vs. one shot ML receiver (designed for nondis- persive channel) performance comparison for system operating at 3 Mbps and with geometry $\theta_1 = 90^\circ$ , $\theta_2 = 90^\circ$ , $\phi_1 = 40^\circ$ and $\phi_2 = 90^\circ$ as distance varies. The solid lines are MLSE BER performance, the dashed lines are the one shot ML decoder BER performance and the dashed line with + marker is the path loss. . . . .	87
4.13	MLSE BER performance vs. transmitter beam-width $\phi_1$ for a system operating at 3 Mbps, $P_t=-5$ dBW and various geometries.	89
4.14	MLSE BER performance vs. receiver FOV $\phi_2$ for a system operating at 3 Mbps, $P_t=-5$ dBW and various geometries. . . .	89
4.15	MLSE BER performance vs. transmitter inclination $\theta_1$ for a system operating at 3 Mbps, $P_t=-5$ dBW and various geometries.	90
4.16	MLSE BER performance vs. receiver inclination $\theta_2$ for a sys- tem operating at 3 Mbps, $P_t=-5$ dBW and various geometries.	91
4.17	Top view of a spatially multiplexed system with two narrower transmit and receive beams instead of a larger beam. . . . .	92
4.18	MLSE BER performance for the 2X2 spatial multiplexing case vs. the SISO case for different SISO transmitter beam an- gles/azimuth skew between MIMO narrower transmitters. . . .	93

4.19	MLSE BER performance for the 2X2 spatial multiplexing case vs. the SISO case for different SISO transmitter beam an- gles/azimuth skew between MIMO narrower transmitters. . . .	94
------	----------------------------------------------------------------------------------------------------------------------------------------------------------------------------------------	----

# Acronyms

APD	avalanche photodiode
BER	bit error rate
bps	bits per second
DARPA	defense advanced research projects agency
DPSK	differential phase-shift keying
DUVAP	deep ultraviolet avalanche photodetectors
FOV	field-of-view
ICNIRP	international commission on nonionizing radiation protection
IEC	international electro-technical commission
IM/DD	intensity modulation/direct detection
ISI	intersymbol interference

LED	light emitting diode
LIDAR	light detection and ranging
LOS	line-of-sight
MAP	maximum-a-posteriori
MIMO	multiple input multiple output
MISO	multiple input single output
ML	maximum likelihood
MLE	maximum likelihood estimation
MLSE	maximum likelihood sequence estimation
MMSE	minimum mean square error
MSE	mean square error
NLOS	non-line-of-sight
OOK	on-off keying
PMT	photomultiplier tube
PPM	pulse position modulation
RF	radio frequency



rms	root mean square
SDMA	spatial division multiple access
SIMO	single input multiple output
SINR	signal to interference plus noise ratio
SNR	signal to noise ratio
SUVOS	semiconductor ultraviolet optical sources
UGS	unattended ground sensor networks
UV	ultraviolet
ZF	zero forcing

# Chapter 1

## Introduction

With recent advances in ultraviolet (UV) sources and detectors, UV communications, especially non-line-of-sight (NLOS) schemes have received increasing interest for diverse applications. A multiple-input multiple-output (MIMO) system coupled with such NLOS technology makes for ideal communications in environments found in urban canyons and forested regions, while providing improved throughput or reliability. This thesis studies corresponding NLOS scattering channels, communication system performance, and receiver design for the MIMO case.

Based on NLOS communication link geometry and UV signal interaction with the atmosphere, the author develops a numerical integration channel model that describes the path loss and system impulse response. The results are then applied to study performance of a NLOS UV MIMO system,

and to design receiver structures for a number of pointing geometries, for both nondispersive and dispersive channels. The author also investigates the effects of channel delay spread on communication quality, i.e., data rate limitation from the induced inter-symbol interference.

## 1.1 UV NLOS Communications

Wireless optical communication systems convey information using optical wavelengths, which range from infrared, visible light, to UV. When compared to radio frequency (RF) systems, they are advantageous [16] in aspects such as huge unlicensed bandwidth, low-power and miniaturized transceivers, higher power densities, high resistance to jamming, and potential increase in data rate. Thus, both infrared and UV waves are very valuable carriers in wireless optical communications. The large unregulated bandwidth and conditions making them virtually free of multiple access interference make wireless optical communications attractive investments commercially. They also possess inherent security characteristics that make them useful for covert applications [30], [31].

A wireless optical communication link consists of an information source, modulator, transmitter, propagation channel, and receiver [16]. Intensity modulation, on-off keying (OOK) and pulse position modulation (PPM) are

widely used modulation schemes. The modulated light is emitted through an atmospheric channel and is affected by atmospheric turbulence, molecular constituents and aerosols [23], [25]. On the receiver end, the receiver is composed of a lens-focusing and filtering subsystem, photodetector and postdetection processor. Optical lenses and filters use particular wavelength-sensitive materials to extract the desired optical field. Photo-detectors are used to produce current based on the received optical photons. Current can then be converted to a voltage for postprocessing after passing through a load resistor or a more complicated amplification circuit.

Infrared technology has been applied to outdoor [23] and indoor communications [22]. An infrared laser or LED in the line-of-sight (LOS) mode of operation is widely used in wireless optical communication systems [22]. It offers advantages of resilience against severe channel dispersion and since the transmitter can be focused on the detector to increase the collected optical power, it can be used with low power emitters. However, a LOS infrared link is vulnerable to blockage because of no alternative paths [23]. An alternative to this is to use multiple sources or tracking detectors [5], but this increases the implementation cost.

In some application scenarios, a LOS link is not feasible and so NLOS optical systems need to be deployed. The UV communication technology has the potential to tackle above issues due to the favorable characteristics of

UV waves and their unique interactions with practical environmental conditions [33]. UV light, especially that with wavelength below 300 nanometers, scatters strongly in our atmosphere, with  $O_2$  molecules being the principal scattering constituent in clear air. Absorption in the atmosphere is so strong that sunlight incident on the Earth in the mid-UV range is almost completely attenuated at the Earth's surface, rendering the term solar blind to this technology, i.e., it's always dark on Earth at 280 nanometers. Such scattering and absorption thus relaxes stringent pointing, acquisition and tracking requirements at the receiver. Moreover, due to high attenuation by the atmosphere, signals beyond the extinction range can hardly be intercepted, which proves to be a desirable feature for tactical applications. Finally, huge and unlicensed spectrum in the UV band may potentially deliver high rate services.

For conditions in which low-power consumption, low-cost implementation, NLOS operability and security are essential, while range and bandwidth requirements are modest, UV technology is ideal. It may find broad-ranging applications in data communication, surveillance sensor networks, homeland security, unattended ground sensor (UGS) networks and small unit communications in urban terrain environments [41]. The UV NLOS communication system can operate with lower power consumption thus minimizing equipment size and providing low cost equipments.

On the other hand, UV communication systems must abide with eye and

skin safety limits. These limits are governed by the International Commission on Nonionizing Radiation Protection (ICNIRP) [8] and the International Electro-technical Commission (IEC) . Radiation safety limits now in effect for free-space laser transmission are  $0.1 \text{ microwatt/cm}^2$  for continuous exposure, and  $0.5 \text{ microwatt/cm}^2$  for 6-hour exposure. The UV sources contemplated for short-range communication will certainly exceed this near the source, and precautions (eye goggles, protective clothing) must be taken to avoid harmful exposure in experiments as well as in any eventual operational setting. After a distance of a few meters from the source, however, the power of the UV signal diffuses enough to be of little concern. Even though the atmosphere is a significant filter for UV-C radiation, humans are sensitive in this region, and UV systems must be designed with this in mind [49].

## 1.2 Motivation

UV is a promising technology for NLOS optical wireless communications due to unique opportunities for communications and sensing. During the past several years, NLOS communication using the optical scattering properties of UV light has been studied for short-range links, and experimental test beds have been developed. The communication applications have been driven by the US Army, for platoon-level communication where covertness and the

NLOS property are of prime interest. This work in turn has been built upon two decades of propagation physics study, led primarily by MIT Lincoln Labs, and by DARPA's programs in UV sources (SUVOS) and UV detectors (DUVAP), though the latter work has been directed at detection of biological and chemical agents using UV radiation.

The high path loss of a NLOS UV channel imposes unique requirements on the system design to achieve desired performance in range and data rate. Increasing the power is a common and straightforward method to improve communication performance, but such an optical communication system must consider the regulations related to human eye safety. Also, the convenience of deployment favors light-weight and compact transceivers. Efficient and sensitive devices such as UV light emitting diodes (LEDs) [36], avalanche photodiode (APD) [3] arrays, and adaptive optics are all among the options of interest to achieve this goal. Recently, the performance of NLOS UV link for communications based on point-to-point transmission has been addressed in [19].

The leading motivation of the research on NLOS UV communications is to study limits on data rate, range, or both, and determine if this technology has potential applications. The system performance strongly depends on the detector characteristics at the receiver end, as well as the received signal power as a function of the channel path loss. In the first part of the work,

we focus on modeling the UV NLOS channel impulse response and analysis of its link performance. For system and network analysis, link loss models in very simple forms are desirable and thus developed in this work.

For a UV NLOS system, the received power to first order is unaffected by the transmit beamwidth as long as the FOV is large enough to see the entire column (or cone) of scattered light [48]. In fact, in the absence of background radiation it is always advantageous to have the receiver FOV angle large enough so that it encompasses the transmit beam at the point of intersection [48]. This suggests that for a fixed large receiver FOV, the system performance would be similar if the transmit array projects a set of narrow beams onto the sky or if the LED array projects one broad beam. If the receiver FOV is narrow, then narrow transmit beams are needed. Potential benefits can be obtained in power gain or multiuser separation by aiming each narrower LED beam onto a different portion of the sky and narrowing the FOV, thereby partitioning the transmit/receiver NLOS paths into near orthogonal channels. Since UV NLOS communications rely on directed communications, it is possible to sector the scattering atmosphere into non-overlapping volumes defined by the transmit/receive angles and using this as a multiplexing technique to provide higher gain and signal to interference rejection. For spatial multiplexing, i.e., the MIMO case, usually the intended receiver and interfering transmitters are in a noncoplanar geometry. It is of



interest to develop UV channel models for noncoplanar geometries. PMT and APD based receiver structures for short range NLOS UV communications need to be developed and the tradeoffs of data rate, range and error performance evaluated.

A key feature of MIMO systems is the ability to turn multipath propagation, traditionally a pitfall of wireless transmission, into a benefit for the communication system. A MIMO communication system needs to be studied for the NLOS UV technology, since it offers potential benefits in power gain or multiuser separation. These benefits can be realized by aiming each transmitter beam onto a different portion of the sky and narrowing the receiver FOV, thereby partitioning the transmit/receiver NLOS paths into near-orthogonal channels. In the presence of channel fading for RF communications, space-time coding can be used to add diversity to the transmission and dramatically improve the performance. Such a MIMO system can also be studied for the UV NLOS communication configuration. Subsequently the performance of receiver structures can be evaluated for various data rates, ranges and system configuration constraints. In the second half of the work, based on an appropriate model for the UV NLOS scattering channel, this research also focuses on developing receiver structures for a simple 2X2 MIMO case.

## 1.3 Literature Review

This literature review consists of articles and books that we found particularly relevant to our work. Other references are introduced at opportune times throughout the thesis. The topics of this work encompass UV NLOS channel modeling, loss analysis, receiver design and performance analysis as constrained by transmitted power, system configuration and communication data rates. The cited papers are related to these topics, and provide the background for the research.

Study on NLOS UV communications started decades ago, dating back to 1960. The concept of exploiting the absence of solar background radiation and the strong scattering at UV wavelengths to realize NLOS communication links was first published in [42]. A number of demonstration systems were subsequently pursued but never fielded, due in part to limitations of source technology, as well as operational concepts that demanded minimal operational ranges of several kilometers [7]. Sunstein used a Xenon flashtube as a UV source to radiate waves of continuous spectrum with shortest wavelength of 280 nm at high power. The PMT based receiver was separated from the transmitter by a 26 km range, resulting in an equivalent NLOS propagation path of 40 km. The performance of this NLOS link was tested for the experimental path geometry. This was followed by Reilly's work with a pioneering

analysis that developed a theoretical channel response model to describe the temporal characteristics of scattered radiation in the middle UV wavelengths of 200-300 nm [32]. Reilly showed that total scattering from molecular and aerosol components dominates at longer wavelengths while absorption dominates at shorter wavelengths. A NLOS UV system based on an isotropic radiating mercury arc lamp at a modulation rate of 40 kHz was demonstrated [14], and later an improved UV local area network test-bed spanning a kilometer range based on a collimated mercury-xenon lamp was built to increase modulation rates up to 400 kHz at an effective wavelength of 265 nm [30]. A UV laser communication system at 266 nm that radiated short pulses at high peak power was also reported in [7] with a data rate of 600 Hz. However, the available UV sources at that time could not meet the need of potential applications because of their large size, high power consumption and unaffordable cost. Thanks to DARPA's SUVOS program launched in 2002, small size, low power and low cost UV LEDs were developed. This progress revived UV communication research and enriched UV applications in other areas as well, such as sensing and water purification.

At the beginning of the rebirth of UV communication research, Shaw et al. made valuable contributions to this field: from concept introduction, link measurement, testbed implementation, to performance evaluation and range extension [40], [38], [37], [39]. Later, multiple access interference in

a NLOS UV sensor network was studied [24]. Chen et al. further evaluated LED based UV communication links experimentally [8], [9]. Xu et al. made a high-fidelity approximation to attain a closed-form solution [48]. The model was further extended to accommodate multiple scattering events for sensor network and communication channel modeling [8], [11], [24], similar to backscattering LIDAR [18]. Ding et al. proposed a parametric single scattering channel model for both impulse response and path loss [10].

The most viable modulation/detection scheme in UV communication is intensity modulation and direction detection (IM/DD) [22]. Several possible modulation schemes are discussed by Kahn and Barry for infrared communication. However, NLOS UV link path loss is very high [48], causing difficulties in achieving satisfactory performance with on-off keying (OOK) modulation. At the detector side, the OOK signal requires a threshold based decision scheme to detect, where the optimal threshold needs to be adapted to SNR. This requirement results in a complex receiver design [26], [34]. Signal detection can rely on a maximum likelihood (ML) detector to achieve optimal performance for the fading case [19]. The authors of [48] utilize an empirical path loss model proposed and analyze the bit error rate performance of short-range NLOS ultraviolet communication receivers.

We look into modeling different receiver structures for the MIMO NLOS UV communication system for both a nondispersive channel case, and chan-

nels with ISI. Xu et al. evaluated the performance of a symbol-by-symbol detector semi-analytically based on the measurement data from their UV NLOS testbed in [8]. In [44], M-ary pulse position modulation (PPM) modulation was adopted and a photomultiplier tube (PMT) was considered as a detector. We further the prior research by constructing receivers for the ISI case for a 2X2 MIMO UV NLOS channel. A classic MLSE receiver for ISI channels and additive white Gaussian noise was developed by Forney in [15] and, based on the same theory, we develop trellis structures based on different amounts of ISI due to the channel for shot noise limited channels.

First investigations that exploit space and angle diversity by MIMO transmission in an optical wireless link were presented by Alqudah et al. in [2] using multibeam forming transmitters and multiple apertures or sectorized receivers. For shorter range systems, [21] shows a MIMO approach to modeling an indoor system. A spatial processing technique that does not require tight spatial alignment, developed for optical wireless MIMO links, was studied in [20], along with the study of the capacity of a MIMO system. In this technique, the interference between spatial channels is modeled and used in communication system design directly to provide high spectral efficiency. Alternatively, interference can be minimized by allowing only a single laser element to transmit, as proposed in [28], or by using interference cancelation techniques at the receiver [43]. In [17], work on space-time codes for MIMO

systems is detailed. [29] reports some preliminary experiments with a simple MIMO interconnect. None of these works address the problems specific to NLOS UV systems, namely high loss, ISI and signal dependent shot noise.

## 1.4 Thesis Outline

The organization of this thesis is as follows.

In Chapter 2, we consider propagation and channel modeling in the context of NLOS deep UV communications. We propose a numerical method using numerical integration. In this approach, the space is divided into small cubic volumes and the received energy from each volume and its arrival time are calculated. The impulse response is calculated based on these time samples using a kernel function. The results obtained using the numerical integration are compared with Reilly's results [27] for different system configurations.

Chapter 3 develops receiver design techniques for the 2X2 MIMO UV NLOS communication system by approximating the channel as a nondispersive channel. The bit error rate performance of the three receivers designed: the zero forcing receiver, the minimum mean square error (MMSE) receiver and the maximum likelihood receiver (ML) are measured for 2X2 MIMO systems.

Chapter 4 focuses on the dispersive UV NLOS channel and develops the maximum-likelihood sequence estimation (MLSE) receiver, which achieves the minimum word error probability for the 2X2 MIMO UV NLOS case. The complexity of the MLSE receiver grows exponentially with the channel response length so we also look into designing a maximum-a-posteriori (MAP) one shot receiver that has prior information about the channel ISI. The bit error performance of the designed receiver is analyzed for a number of UV NLOS geometries and data rates. The advantage offered by spatial multiplexing is investigated.

Chapter 5 concludes the thesis, and also indicates possible future research directions.

## Chapter 2

# Ultraviolet NLOS Channel

## Modeling and Loss Analysis

We consider propagation and channel modeling in the context of NLOS deep UV communications. A computationally flexible numerical integration approach is presented that can be used to generate the UV scattering channel impulse response and path loss evaluation for noncoplanar geometries. This approach lays the foundation for efficiently modeling the UV NLOS MIMO system.

Many techniques have been presented to accurately model the NLOS UV channel. A simulation approach using a Monte Carlo method is presented in [11] and [13] for single scattering and multiple scattering interactions, respectively. An analytical approximation can be remarkably helpful for



getting a fast initial scope of the link performance. In [27] Luetttgen et. al. present an analytical model for the impulse response integral form by considering only the single scatter propagation. An approximate closed form path loss for NLOS UV links with small transmitted beam-widths and small fields of view (FOV) is calculated in [47]. In [48], the common volume between the transmitted beam and receiver FOV is approximated by a frustum and, in this way, a closed form expression for path loss is obtained. A popular single scattering channel model [47] reliably predicts observed propagation with  $1/r$  range dependent power decay for very short range  $r$  (on the order of meters) and large apex angles for the transmitter and receiver. Recently, another approximate link loss is calculated in [45] for noncoplanar geometries.

We propose a simulation method using numerical integration. In this approach, the space is divided into small cubic volumes and the received energy from each volume and its arrival time are calculated. The impulse response is calculated based on these time samples using a kernel function. The path loss is calculated as the ratio of the transmitted energy to the total received energy from all small volumes. The numerical integration technique provides advantages of scalability and flexibility for all transmitter-receiver pairs while also accounting for shadowing due to obstructive objects in the system. For a fixed distance, the numerical integration approach involves calculating a system configuration independent loss factor, which can be used

to calculate the loss due to any transmitter( $T_x$ ) to receiver( $R_x$ ) geometries. This is compared to the analytical approach in [27], which, although faster, cannot incorporate shadowing effects in the system model. A comparison is also drawn with the Monte Carlo approach as described in [13].

The proposed numerical integration approach is computationally efficient when compared to the Monte Carlo approach. The algorithm complexity is lower than for the Monte Carlo approach for the same number of trials or cubes. The proposed method is even more computationally efficient when used for the MIMO case. Using the numerical integration method, a path loss matrix is generated for a fixed distance once, and any number of transmitter or receiver pairs can then be superimposed on this path loss matrix with their individual gains to calculate path losses and receive powers.

## 2.1 Numerical Integration Approach for Link Loss

Even though the numerical integration approach is flexible for other assumptions, we consider a somewhat idealized model of the communication channel, following the framework of [49] and [48]. Suppose a UV transmitter directs radiation within an ideal circular cone having cone angle  $\phi_1$  with elevation

angle  $\theta_1$  and an azimuth angle of  $\alpha_1$ , as illustrated in Fig. 2.1. Light within this cone is scattered from natural atmospheric particles and other aerosols. Also imagine a receiver whose detector has a field of view, or acceptance region, modeled by an ideal cone with angle  $\phi_2$ , elevation angle  $\theta_2$  and azimuth angle  $\alpha_2$ . To first-order, these two overlapping cones define a common scattering volume  $V$  in the sky, and only energy scattered from within this volume is considered as captured by the receiver.

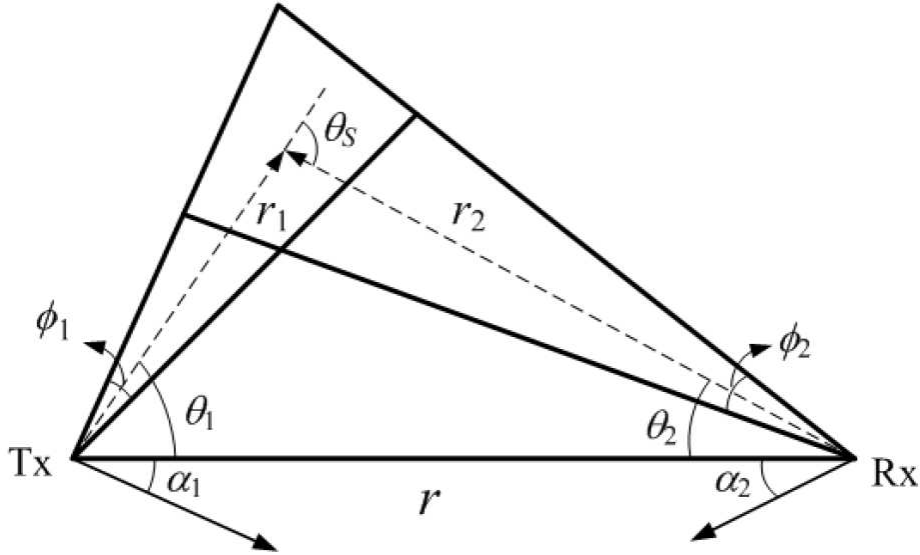


Figure 2.1: Geometry of the NLOS UV link.

Let  $E_t$  denote transmitted pulse energy,  $\Omega_1$  the transmitter solid angle in steradian, and  $A_r$  the receiver collecting aperture.  $r$  denotes the transmitter ( $T_x$ ) to receiver ( $R_x$ ) baseline separation, and  $r_1$  and  $r_2$  denote the distances of the common volume to the  $T_x$  and  $R_x$ , respectively.  $\theta_s = \theta_1 + \theta_2$  is the

angle between the forward direction of the transmitted waves and the receiver axis.

To calculate the total energy received for all transmitter and receiver geometries, we divide the volume enclosing the transmitter and receiver pair into smaller cubical differential volumes ( $\delta V$ ). There are two steps towards calculating the received energy. First, the energy scattered by any small cube is computed, then the transmitter beam shape and receiver FOV (antenna gain) is included. For an isotropic transmitter and receiver pair, each of these cubical volumes contributes to a differential energy ( $\delta E_r$ ) at the receiver given by [27]. To take into account the system geometry and beam parameters, both the transmitter and receiver are modeled using gain factors  $G_t$  and  $G_r$  respectively. The receiver is modeled with a Lambertian acceptance profile. For all angles within the field of view  $\phi_2$  of the receiver, a receiver Lambertian gain  $\delta G_r$  is observed as  $\delta G_r = \cos(\xi)$ , where  $\xi$  is the angle between the receiver axis and the vector from the center of each differential volume to the receiver.

Hence, for each  $\delta V$ , the receiver now detects effective energy  $\delta E_e$  (in joules) given by  $\delta E_r \times \delta G_t \times \delta G_r$ . Thus, once we calculate the received energy  $\delta E_r$ , which is fixed for a particular transmitter to receiver distance, it can be multiplied by the transmitter and receiver gains for different geometries to provide actual energy received from each  $\delta V$ . The total energy received is the total contribution of all such energies corresponding to each of the

differential volumes integrated over the common scattering volume  $V$

$$E_r = \int_V \delta E_r \times \delta G_t \times \delta G_r. \quad (2.1)$$

At time  $t = (r_1 + r_2)/c$  (where  $c$  is the speed of light), a differential volume ( $\delta V$ ) contributes differential energy (in joules/m<sup>3</sup>) at the receiver given by [27]

$$\delta E_r = \frac{K_s E_t P(\mu) A_r \delta V}{r_1^2 r_2^2} e^{-K_e(r_1+r_2)}. \quad (2.2)$$

All differential geometry parameters used in this equation are calculated with respect to the center of each of the differential cubes. This differential energy per solid angle received is based on the assumption of an isotropic transmitter and receiver pair. The scattering coefficient,  $K_s$ , is a function of wavelength and the scattering angle  $\theta_s$ . The exponential extinction coefficient,  $K_e$ , is the sum of  $K_s$  and the absorption coefficient,  $K_a$ .  $K_s$  is given as  $K_s = K_s^{Mie} + K_s^{Ray}$ , where  $K_s^{Mie}$  is the scattering coefficient due to Mie or aerosol scattering, and  $K_s^{Ray}$  is the scattering coefficient due to Rayleigh or molecular scattering [32].  $P(\mu)$  is the phase scattering function with  $\mu = \cos(\theta_s)$ . This is modeled as a weighted sum of the Rayleigh (molecular) and Mie (aerosol) scattering phase functions based on the corresponding scattering coefficients [50],

$$P(\mu) = [P_{Ray}(\mu) + \frac{K_s^{Mie}}{K_s^{Ray}} P_{Mie}(\mu)] / (1 + \frac{K_s^{Mie}}{K_s^{Ray}}). \quad (2.3)$$

The Mie scattering phase function is given by a generalized Henyey-Greenstein

function [50]

$$P_{Mie}(\mu) = \frac{1 - g^2}{4\pi} [(1 + g^2 - 2g\mu)^{-3/2} + f \frac{0.5(3\mu^2 - 1)}{(1 + g^2)^{3/2}}] \quad (2.4)$$

where  $g$  is the aerosol asymmetry parameter given by the mean cosine of the scattering angle and  $f$  is aerosol hemispheric backscatter fraction. The Rayleigh scattering phase function is modeled as a generalized Rayleigh model [4]

$$P_{Ray}(\mu) = \frac{3}{4(1 + 2\gamma)} [(1 + 3\gamma) + (1 - \gamma)\mu^2], \quad (2.5)$$

where  $\gamma$  is defined by [6]

$$\gamma = \frac{\rho}{2 - \rho}. \quad (2.6)$$

$\rho$  is the depolarization parameter.

For the transmitter, we consider two cases: one modeling the transmitter beam as a Gaussian profile and the other, modeling the transmitter energy as uniformly distributed over the transmitter solid cone angle. Each differential volume experiences an effective transmitter gain factor  $\delta G_t$ . The transverse gain profile of the transmitter beam modeled with a Gaussian function is given by [35]

$$\delta G_t = \frac{1}{\pi(w_z^2)} e^{-2r_t^2/w_z^2}, \quad (2.7)$$

where the beam radius,  $w_z$ , is the set of points in the  $1/e^2$  contour after the wave has propagated a distance  $z$  along the beam axis, and  $r_t$  is the

transverse distance of the center of each differential volume from the central axis of the beam. The beam radius varies along the propagation direction  $z$  according to  $w_z = w_o(1 + z/z_r)^{1/2}$ , where  $z_r$  is the Rayleigh length and  $w_o$  is the radius of the  $1/e^2$  irradiance contour at the beam waist.

Similarly, for a uniform beam, the gain of the transmitter is given by

$$\delta G_t = \begin{cases} 1/\Omega_t & \text{if } \delta V \in V \\ 0 & \text{otherwise.} \end{cases}$$

where  $\Omega_t$  is the steradian solid angle of the transmitter beam.

## 2.2 Numerical Integration Approach for Impulse Response Calculation

The impulse response of the channel is calculated using the numerical integration approach introduced above. The impulse response is calculated as an energy-delay curve given by the expected energy received through the multipath channel collected over arrival time delay. Similar to the method described earlier for computing the received energy, the volume defined by the  $T_x$  and  $R_x$  beams is divided into many smaller volumes. For each volume, the energy received per unit time is noted versus the time delay for the path between the  $T_x$  and  $R_x$  passing through the center of the differential volume. As illustrated in Fig. 2.1, the time delay  $t$  associated with the cubical volume

at the center of the overlap volume is given by

$$t = \frac{r_1 + r_2}{c}. \quad (2.8)$$

The time delay is divided into time bins and the energies corresponding to same time bins are summed. This energy per unit time versus time delay plot is convolved with a kernel function  $K(t)$ , with standard deviation  $\sigma_k$ , to smooth the discrete differential contributions to the impulse response. To ensure sufficient accuracy in the curve and to minimize contributions due to overlapping tails of each kernel functions, a narrow Gaussian kernel function should be used,

$$K(t) = \frac{1}{\sqrt{2\pi}} e^{-(t)^2 / 2\sigma_k^2} \quad (2.9)$$

We use a standard deviation of the order of 1 nanosecond, which is two orders of magnitude less than the impulse response observed for practical  $T_x$  to  $R_x$  distances.  $\sigma_k$  is three times as large as the time bins used to ensure a smooth curve.

## 2.3 Shadowing Effects Due to Obstacles

In NLOS communication settings, shadowing is caused by the appearance of large objects, such as buildings or walls, between the transmitter and the receiver. Unique properties described earlier make UV communication



a candidate for military and civil applications in situations where obstacles, such as mountains and buildings, often exist. Such obstacles can reduce the received signal strength and may adversely affect the communication link. Consequently, it is important to study the effects of obstacles on UV communication links. However, the effects caused by obstacles in UV communication, such as the decrease in the received energy density, the best elevation angles for the transmitter and receiver, etc., are not well studied in literature.

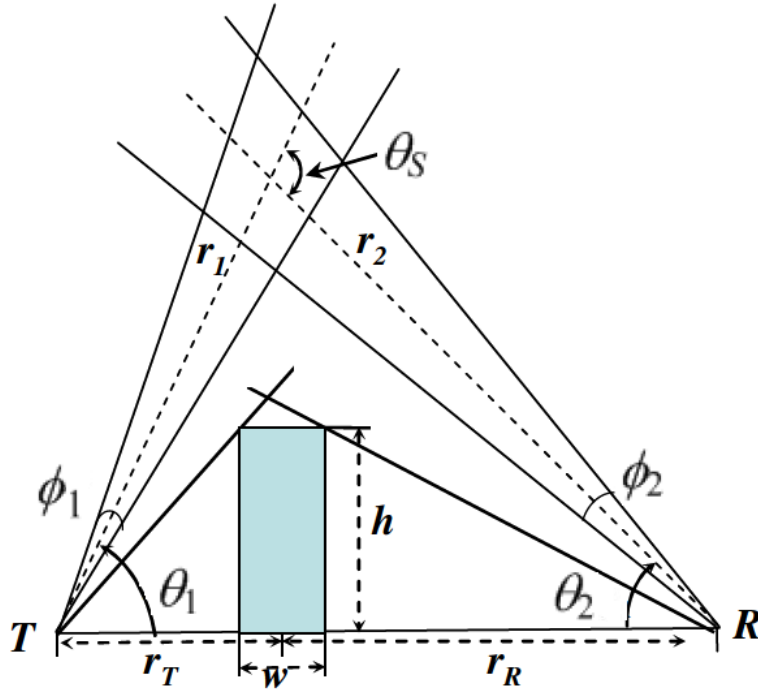


Figure 2.2: Shadowing due to obstacles in a NLOS UV link geometry. Figure modified and taken from [51].

We use the numerical integration approach derived above to study the effects of obstacles on NLOS UV links. As shown in Fig. 2.2, the obstructing object has dimensions  $w$  metres  $\times$   $h$  metres  $\times$   $d$  metres. The object lies at a distance of  $r_T$  from the transmitter and  $r_R$  from the receiver. In order to incorporate the effect of obstacles on the link, we model the volume occupied by the obstacles as corresponding to zero gain. Furthermore, all differential volumes whose lines of sight to the transmitter and the receiver are blocked by the obstacle contribute zero to the received energy. This provides an additional computational advantage of our approach, because the numerical integration can now be done on a subset of the original volume, i.e., the received energy and delay is calculated for cubes that have an unobstructed line of sight view of both the transmitter and the receiver. Although Fig. 2.2 shows the object lying between the line of sight of the  $T_x$  and the  $R_x$  pair, the numerical integration approach can account for an object of any dimension and spatial position.

## 2.4 Numerical Results

In this section numerical results for the impulse response and path loss are presented and compared to results from previously proposed methods.

Fig. 2.3 shows the impulse responses for a case where the transmitter

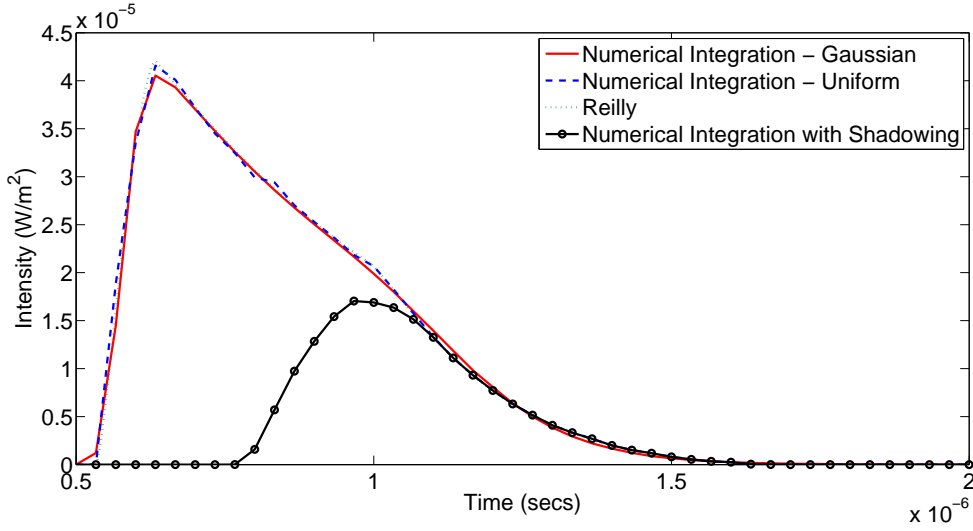


Figure 2.3: Impulse response for  $\theta_1 = 90^\circ$ ,  $\theta_2 = 45^\circ$ ,  $\phi_1 = 17^\circ$ ,  $\phi_2 = 30^\circ$ , and  $d = 100$  m using Reilly's approach [27] and the numerical integration method. Numerical integration is plotted for both uniform and Gaussian transmitted beams, and also for a case including shadowing.

beam is pointed vertically upwards. For the numerical integration method, we have plotted two cases, one for the uniform transmitted beam and the other for the Gaussian beam. All results are obtained assuming only single scatter interactions. The Gaussian and uniform beams give almost identical results in this case, with the rms delay spread of the channel measured to be  $0.42 \mu\text{s}$ . A receiver area of  $1.77 \text{ cm}^2$  is assumed and the space is divided into 42M cubes, each of size  $0.008 \text{ m}^3$ . A wavelength of 260 nm is used, with  $K_e = 0.79 \text{ km}^{-1}$  and  $K_s = 0.91 \text{ km}^{-1}$ . The impulse response curve for the Gaussian transmitter appears to rise earlier because the volumes outside of

the transmitter main beam-width contribute some received energy due to the non-zero transmit gain for such volumes.

Fig. 2.3 also shows the effects of shadowing on this configuration by displaying the impulse response curve obtained when a building of dimensions  $30\text{ m} \times 20\text{ m} \times 35\text{ m}$  (length  $\times$  width  $\times$  height) is at a distance of 40 m from the  $T_x$ . The length of this building is along the  $T_x$ - $R_x$  axis, the width is perpendicular to this axis on the ground plane, while the height is the vertical reach of the building. This tall building's shadow nearly halves the transmitter energy, as shown by the lower area under the impulse response curve for this case. The curve appears delayed since this building blocks shorter delay paths for the given configuration, and the energy received is through the longer delay paths. One inadvertent benefit of shadowing is therefore a smaller delay spread which can offer data rate advantages if exploited appropriately. The rms delay spread for this curve is  $0.28\text{ }\mu\text{s}$ .

Fig. 2.4 shows the impulse responses for a case where the coplanar transmitter and receiver beams are inclined at slightly lower angles. Note the more pronounced differences in the impulse response curves as generated by the three different methods. The Gaussian beam curve rises earlier again and is slightly higher in peak value since the beam is now modeled with a Gaussian profile and the common volume between the transmitter and the receiver beams is lower. Using the same number and size of cubes as used previously,

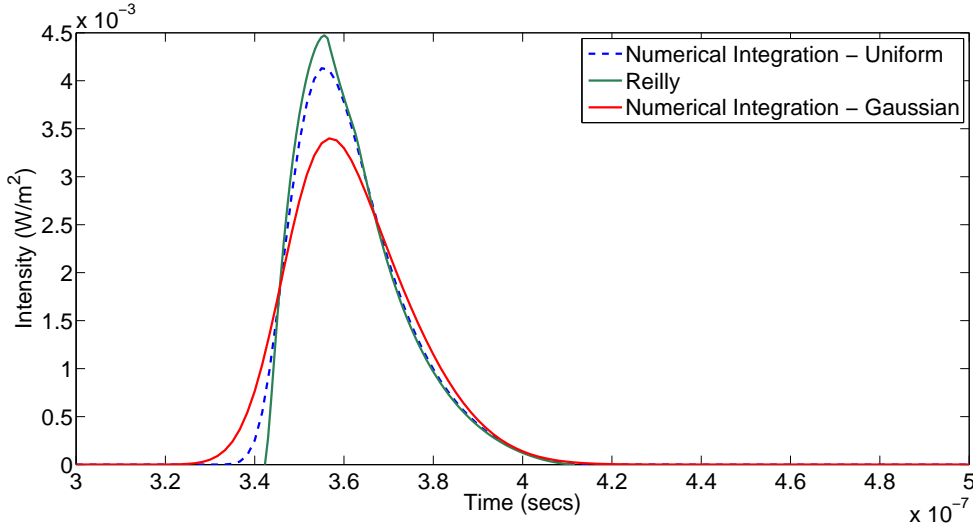


Figure 2.4: Impulse response for  $\theta_1 = 20^\circ$ ,  $\theta_2 = 30^\circ$ ,  $\phi_1 = 17^\circ$ ,  $\phi_2 = 30^\circ$ , and  $d = 100$  m using Reilly's approach [27] and the numerical integration method. Numerical integration is plotted for both uniform and Gaussian transmitted beams.

this approximation leads to the slight difference in Gaussian beam impulse response. The difference between the uniform and the Reilly approaches is slight, as both these methods give almost the same channel loss values (area under the impulse response curve). The rms delay spread of the channel as given by all three approaches is around 23.4 ns.

The path loss of the NLOS UV link is illustrated in Fig. 2.5 for high inclination angles for both the transmitter and receiver beams. The path loss is plotted for measurement from [48], the Monte Carlo method incorporating multiple scatterings [48] and our proposed numerical integration method. As

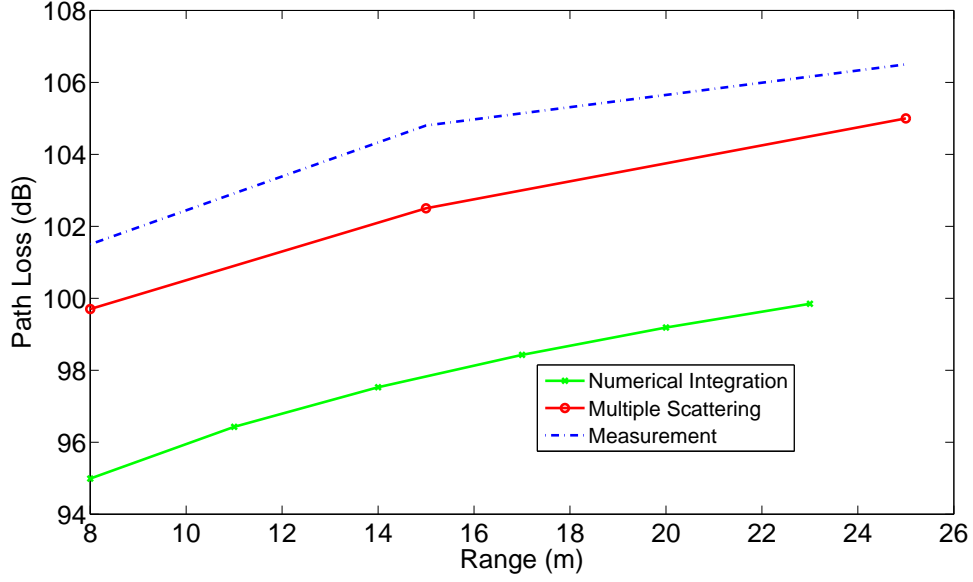


Figure 2.5: Path loss vs. range for  $\theta_1 = 80^\circ$ ,  $\theta_2 = 60^\circ$ ,  $\phi_1 = 10^\circ$  and  $\phi_2 = 30^\circ$ , using different methods.

can be seen, the path loss using the numerical integration is lower than the path loss predicted by [48], since the numerical integration method is single scattering based. The difference between the measurement results and the other results in all figures can be because of model oversights, for example, modeling a real situation, or the effect of some unmodeled parameters.

Fig. 2.6 shows the path losses for a geometry with low transmitter and receiver beam angles. The measurement results and Monte Carlo results are taken from [11]. In Fig. 2.7, the path losses from the various methods are plotted for a different set of low transmitter and receiver beam angles, using

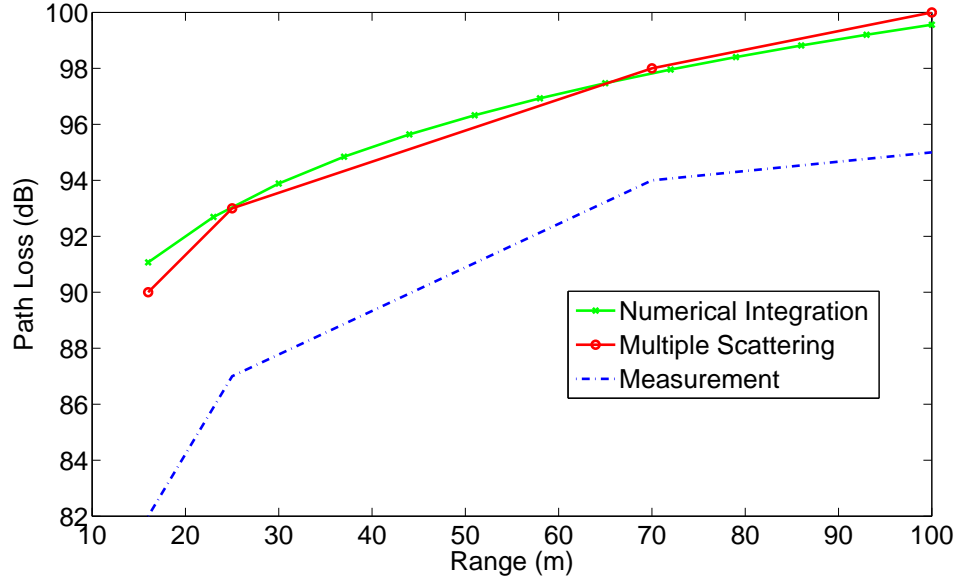


Figure 2.6: Path loss vs. range for  $\theta_1 = 20^\circ$ ,  $\theta_2 = 30^\circ$ ,  $\phi_1 = 17^\circ$  and  $\phi_2 = 30^\circ$ , using different methods.

the same scattering and extinction coefficients as for Fig. 2.6. The path loss results from numerical integration are remarkably close to those obtained from the Monte Carlo simulation technique that incorporates multiple scattering exactly. The measurement and Monte Carlo path losses are plotted in Fig. 2.7 using results from [11].

Fig. 2.8 shows the effects of azimuth skew between transmitter and receiver beams. The path loss is minimum when beams are coplanar since both the transmitter and receiver beams observe a maximum overlap. A skew from a noncoplanar geometry decreases the overlap volume, and hence

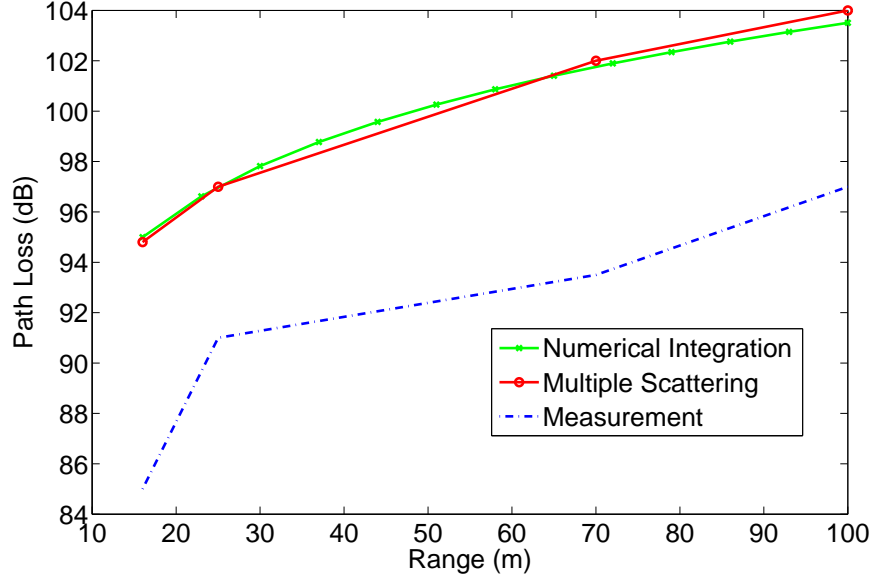


Figure 2.7: Path loss vs. the range for  $\theta_1 = 40^\circ$ ,  $\theta_2 = 20^\circ$ ,  $\phi_1 = 17^\circ$  and  $\phi_2 = 30^\circ$ , using different methods.

the received power. It is interesting to note that the path loss increases rapidly with skew for smaller transmit and receive beams, which indicates the need for better pointing in such cases. Larger receiver beams not only capture more power but relax pointing requirements.

We see that pointing requirements can be relaxed by using larger receiver beams. If we exploit spatial diversity by splitting the transmitter beam into two narrower beams pointing to the same region, we observe that pointing requirements are relaxed even further. This is shown in Fig. 2.10 where instead of the original transmitter with beam width  $\phi_1^{ISO} = 40^\circ$ , the system



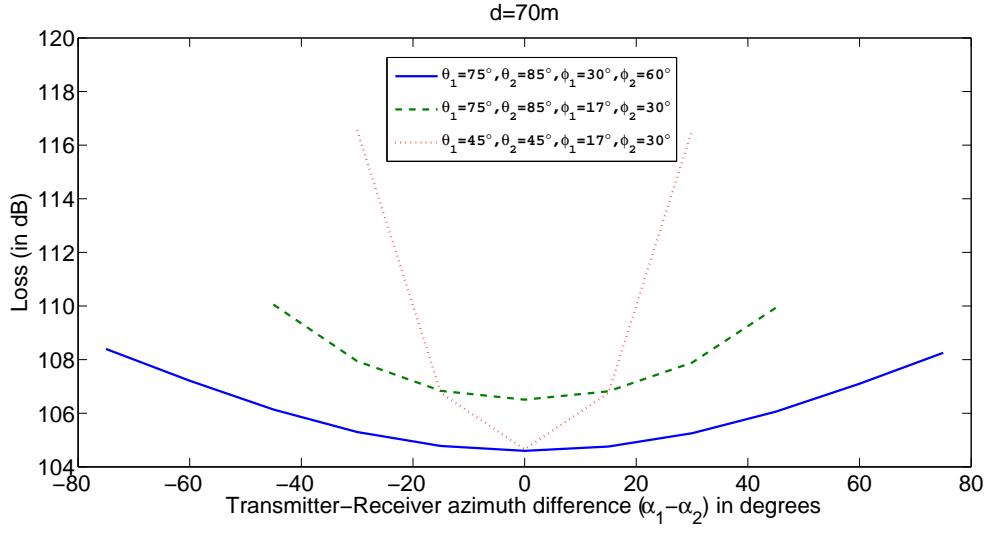


Figure 2.8: Path loss vs. transmitter to receiver azimuth skew for different geometries.

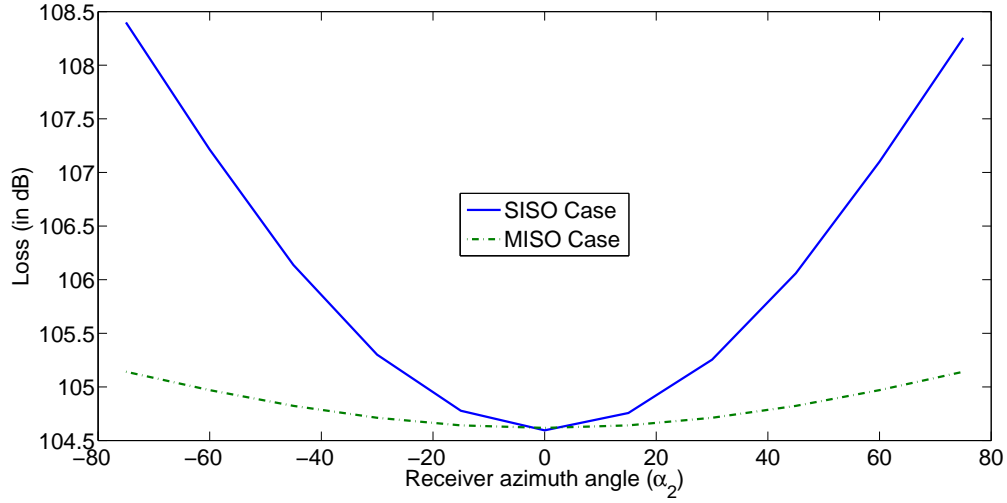


Figure 2.9: Path loss vs. transmitter to receiver azimuth skew for spatial multiplexing case.

uses two transmitters with beam widths  $\phi_1^{MISO} = 10^\circ$ , and at an azimuth difference of  $\phi_1^{SISO} - \phi_1^{MISO}$  with each other as shown in Fig. 2.9. The receiver beam is now more likely to overlap with the split transmitter beams and get more power even when it is not pointed correctly. We see that using spatial diversity, the loss remains nearly constant even in the case of a large receiver azimuth skew. Thus, using multiple transmitters to transmit data on narrower beams leads to less path loss and relaxes pointing requirements even further.

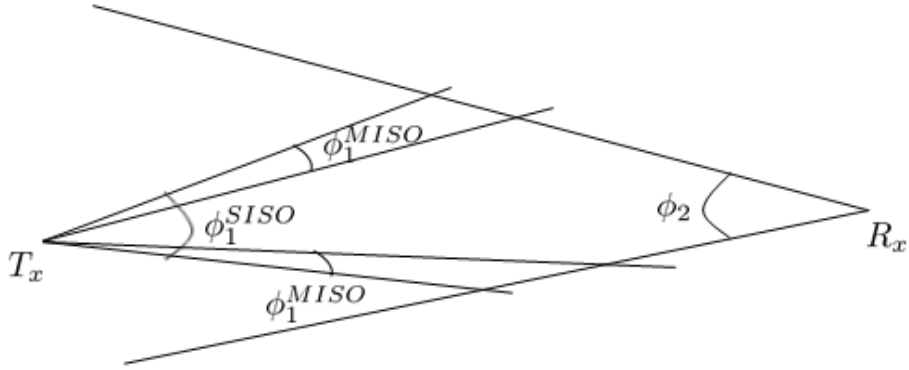


Figure 2.10: Top view of a spatially multiplexed system with two narrower transmitter beams instead of a larger beam.

## 2.5 Computational Complexity

The Monte Carlo approach as described in [13] can deal with both noncoplanar geometries and shadowing but requires more computations for a similar accuracy. We implement the numerical simulation using a composite midpoint rule for integrating over the large volume  $V$  the energy  $\delta E_r$  due to each of the differential volumes  $\delta V$ . The error of this algorithm is upper bounded by  $O(N^{-2/3})$  and its complexity is given by  $O(N)$ , where  $N$  is the total number of differential volumes making up the space encompassing the system. Typical values of  $N$  that were used in the simulations were on the order of  $10^6$ . This method provides higher accuracy for a similar number of trials when compared to the Monte Carlo simulations in [13]. For  $P$  trials, the Monte Carlo simulations in [13] are complexity bounded by  $O(P)$  with the error order of convergence as  $O(P^{-1/2})$ . Thus, for the same computational overhead, better accuracy is achieved using the numerical integration approach.

An added advantage of the numerical integration approach is its flexibility in dealing with MIMO systems. Using this approach, the received energy matrix for each cube ( $\delta E_r$ ) needs to be calculated only once, after which the receiver and transmitter gains ( $\delta G_t, \delta G_r$ ) can be superimposed for any number of transmitters and receivers. This reduces the computational over-

head significantly. Moreover, for larger distances, the whole system can be scaled by using the same number of cubes but now with a larger dimension. This makes the numerical integration method more convenient to use even for different distances.

## 2.6 Chapter Summary

In this chapter, simulation modeling methods are proposed for the NLOS UV system. Using the numerical integration technique, we compute the total received energy for different  $T_x$  and  $R_x$  geometries varying by elevation, beam, azimuth angles and transmitter-receiver distance. This technique is computationally efficient and can provide extra flexibility by accounting for noncoplanar  $T_x$ - $R_x$  geometries as well as shadowing in the system due to objects obstructing the propagation path between the transmitter and receiver. This shadowing factor can be incorporated in the transmitter and receiver gain terms, and provides an added advantage over the analytical approach in [27]. The proposed method provides for convenient path loss and impulse response analysis for MIMO systems, which gives it a unique edge over methods already documented in literature. Pointing requirements for UV NLOS systems are stringent for narrow beams since misdirected transmitter-receiver pairs increase path loss significantly. Spatial multiplexing provides a solution

to this problem. Multiple narrow transmit beams can be used to ensure overlap with the receiver beam even in cases of high transmitter-receiver azimuth skew. The impulse response and path losses from the proposed approaches are compared to several previously presented techniques. The results obtained using the numerical integration are shown to be in agreement with the Reilly results for different system geometries.

# Chapter 3

## Receiver Design for Nondispersive Channels

NLOS UV communication links endure a variety of degradations, including scattering and absorption caused by molecules and aerosols. The channel impulse and frequency responses allow us to determine how severe the pulse temporal spread is. These responses are critical for selecting system design parameters such as data rate, modulation and demodulation schemes. Although the scattering enables NLOS links, this is achieved at the penalty of high path loss. For most UV communication applications envisioned, the path loss cannot be readily overcome by using more transmit power due to human eye and skin sensitivity and the corresponding exposure safety limits. This challenge motivates the current study, in which range extension for

NLOS UV communications is considered, aided by studying receiver design techniques is considered. In this chapter, we focus on data rate, and characterize operational range and associated tradeoffs in receiver design when the channel is nondispersive. We consider the dispersive case in the next chapter.

In this chapter, we also examine the possibility of using the optimum receivers for power gain and multiuser separation by aiming each narrower LED beam onto a different portion of the sky and narrowing the FOV, thereby partitioning the transmit/receiver NLOS paths into near orthogonal channels.

### 3.1 Channel Path Loss Model Description

In this section, we first introduce our channel path loss model. With intensity modulation and direct detection, the detected optical power  $y(t)$  can be regarded as the convolution of the transmitted optical signal  $x(t)$  and the UV NLOS channel intensity impulse response  $h(t)$ , corrupted by noise  $n(t)$  at the receiver, as given by

$$y(t) = x(t) * h(t) + n(t). \quad (3.1)$$

where  $x(t)$  is a power limited signal, with  $0 \leq x(t) \leq A$ ,

$$\lim_{T_s \rightarrow +\infty} \frac{1}{2T_s} \int_{-T_s}^{T_s} x(t) dt \leq P_t. \quad (3.2)$$

$T_s$  is the symbol time,  $P_t$  is the average power for each symbol, and  $n(t)$  represents the noise effect due to dark current, thermal noise and shot noise at the receiver.

The UV signal undergoes absorption, scattering and turbulence effects. To establish the link budget, it is necessary to characterize the channel path loss model, which can be treated as the reciprocal of channel DC gain  $H(0)$  given by,

$$H(0) = \int_{-\infty}^{+\infty} h(t) dt. \quad (3.3)$$

The received average optical power is thus  $P_r = P_t \times H(0)$ . In addition, the channel total delay spread (the duration of  $h(t)$ ) affects communication performance because it induces inter-symbol interference (ISI) as the pulse rate increases. ISI is not critical when the symbol time is much longer than the delay spread, i.e., when the system operates at low rate. As shown in the previous section, for the configuration with  $\theta_1 = 20^\circ$ ,  $\theta_2 = 30^\circ$ ,  $\phi_1 = 17^\circ$ ,  $\phi_2 = 30^\circ$  and  $d = 100$  m, UV channel delay spreads are of the order of 100 nanoseconds. Hence for low data rates ( $\sim 100$  Kbps and less than 1 Mbps), the channel delay spread is assumed to be negligible compared with



the symbol duration.

We rely on path loss to predict the received signal to noise ratio (SNR). The SNR, along with the relevant source and detector statistics, leads to probability of error expressions, which serve as the basis for predicting the maximum communication range.

### 3.2 Receiver Description and Noise Model

Assuming OOK intensity modulation and a direct detection receiver (OOK IM/DD), the received backscattered optical power is converted to an electrical current at the detector, which, according to [1], is given by the relation

$$I_p = \Re G P_r, \quad (3.4)$$

where  $G$  is the gain of the receiver and  $\Re$  is the detector responsivity.  $P_r$  is the power (in watts), which is an input to the optical receivers. The responsivity is defined as

$$\Re = \frac{q\eta}{\hbar\nu}, \quad (3.5)$$

where  $\eta$  is the quantum efficiency of the photodiode,  $q$  is the electron charge,  $\hbar$  is Planck's constant, and  $\nu$  is the optical frequency.

Shot noise and thermal noise are the two fundamental noise mechanisms

responsible for current fluctuations in all optical receivers, even when the incident optical power  $P_r$  is constant. Shot noise is a manifestation of the fact that an electric current consists of a stream of electrons that are generated at random times. The shot noise variance,  $\sigma_s^2$ , is obtained as given in [1] by

$$\sigma_s^2 = 2qG^2(I_p + I_d)\Delta f. \quad (3.6)$$

where  $\Delta f$  is the effective noise bandwidth of the receiver, set equal to twice the data rate, and  $I_d$  is the dark current in the receiver.

At a finite temperature, electrons move randomly in any conductor. Random thermal motion of electrons in a resistor manifests as a fluctuating current even in the absence of an applied voltage. The load resistor in the front end of an optical receiver adds such fluctuations to the current generated by the photodiode. This additional noise component is referred to as thermal noise.

The thermal noise is defined in [1] as

$$\sigma_{TH}^2 = \left(\frac{4kT_p}{R_{load}}\right)F_n\Delta f. \quad (3.7)$$

where  $k$  is Boltzmann's constant,  $T_p$  is the noise temperature in degrees Kelvin,  $R_{load}$  is the load resistor and  $F_n$  represents the factor by which thermal noise is enhanced by various resistors used in the amplifiers.

Since shot and thermal noises, with variances as described in (3.6) and (3.7), are independent random processes with approximately Gaussian statis-

tics, the total variance of current fluctuations,  $\sigma_n^2$ , can be obtained simply by adding individual variances [1]. The result is

$$\sigma_n^2 = \sigma_{TH}^2 + \sigma_s^2. \quad (3.8)$$

### 3.3 MIMO Model

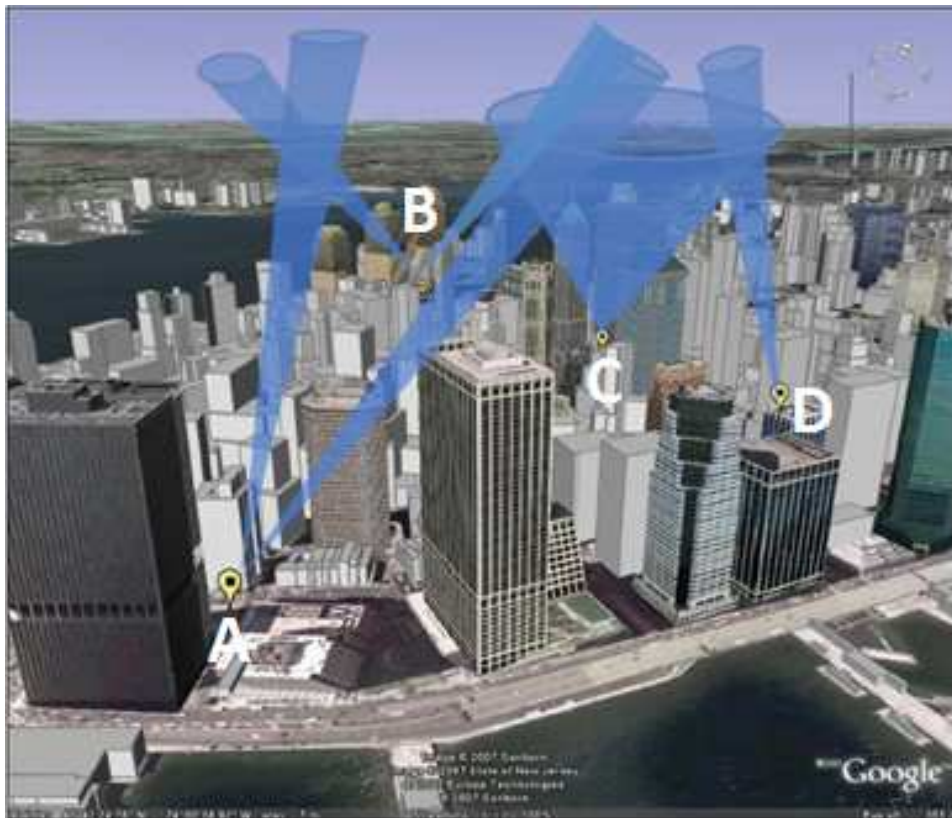


Figure 3.1: UV NLOS MIMO system. Figure taken from [49] and modified.

Multiple-input multiple-output (MIMO) systems have attracted significant research attention in the past decade because they possess the ability to

provide high speed wireless communications over a multipath environment [46]. To maximize the system capacity, different transceivers may be allowed to access a common UV channel simultaneously and independently. In principle, we investigate multiple access using the spatial dimensionality. Notice that spatial division multiple access (SDMA) requires strict directional pointing between transceivers of interest, and can work well in LOS conditions. Under NLOS scattering conditions, however, the overlap of transceiver FOV cones must be controlled. The system geometry dominates access performance.

Such a multiuser system can belong to two types: multiuser systems which are multiple users with single transmit and receive nodes operating independently, and fully MIMO systems for coordinated communications. One multiuser system, which is the SIMO case, consists of a transmitter that has a single beam and the receiver that has multiple beams. Another case for a multiuser system would be where the same data is transmitted redundantly from the two transmitter beams and received by a single receive node, which is the MISO case. The receiver in this case is then able to receive the optimum signal, which it can then use to extract the required data. In Fig. 3.1, nodes A and B form a MIMO system with co-located transmitter and receiver beams. Nodes A, C, D form a multiuser SISO system where a single receiver at node C obtains data from independent transmitters A and

D.

For designing the optimum receivers, we consider a 2X2 MIMO case with 2 transmitters and 2 receivers as shown in Fig. 3.2. For the  $i^{th}$  transmit

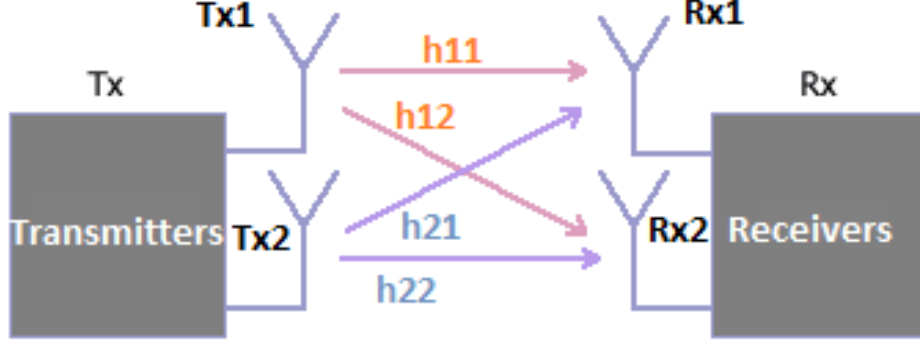


Figure 3.2: UV NLOS 2X2 MIMO system.

antenna to the  $j^{th}$  receive antenna, each transmitted symbol is multiplied by the path loss of the nondispersive channel,  $h_{ij}$ , which is calculated as discussed in (3.3) above.  $x_1(t)$  and  $x_2(t)$  are signals transmitted from transmitters 1 and 2 respectively, where the transmitted signal  $x_i(t)$  is given by  $x_i(t) = \sum_k x_i^{(k)} p_T(t - kT)$ , where  $x_i^{(k)} \in \{0, 1\}$ ,  $T$  is the symbol interval and  $p_T(t)$  is the transmitted signal pulse shape. We consider OOK modulation for the UV NLOS system, so the transmitter pulse shape is a rectangle. The received vector on the first receive antenna,  $y_1(t)$ , and on the second receive

antenna,  $y_2(t)$ , is given by

$$\begin{bmatrix} y_1(t) \\ y_2(t) \end{bmatrix} = \begin{bmatrix} h_{11} & h_{12} \\ h_{21} & h_{22} \end{bmatrix} \times \begin{bmatrix} x_1(t) \\ x_2(t) \end{bmatrix} + \begin{bmatrix} n_1(t) \\ n_2(t) \end{bmatrix} \quad (3.9)$$

where  $n_1(t)$  and  $n_2(t)$  are noise vectors at receiver 1 and receiver 2 respectively, generated due to both thermal and shot noise contributions at each receiver. In order to process the continuous time received signal,  $y_i(t)$ , in discrete time,  $y_i(t)$  is passed through a receive filter designed to provide the maximum signal to noise power ratio at its output for a given transmitted symbol waveform. An integrate-and-dump filter is used instead of a matched filter since the received pulse-shape depends on the channel response and the receiver cannot be easily designed to match it. The integrate-and-dump filter output is sampled at every bit interval,  $T$ , to provide the discrete time signal  $y_i$ .

The discrete time model can be simplified as

$$Y = H \times X + N. \quad (3.10)$$

$H$  is the MIMO channel matrix and  $N$  is the noise vector generated at the receivers for vector  $X$  sent from the transmitters.

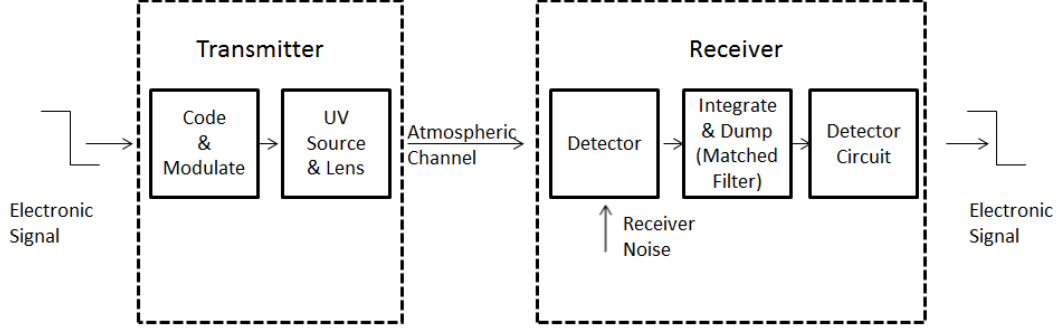


Figure 3.3: UV communication principle diagram.

### 3.4 Receiver Design

The digital source provides symbols to be transmitted. The modulator at the transmitter imprints this digital information onto an optical carrier. The electrical stage of the transmitter drives an optical source to produce modulated light. A semiconductor laser or LED is usually used as the optical source. Currently deployed free-space optical communication systems use OOK with direct detection, and some are beginning to use differential phase-shift keying (DPSK) with interferometric detection. The information carrying light wave then passes through the transmission medium, i.e., the free space optical channel in this system. The wave then reaches the receiver stage where the optical detector receives the optical carrier and outputs electric current. The common types of optical detectors used are photodiodes (p-i-n, avalanche), photomultiplier tubes etc.. Finally the receiver and demodulator act on the

amplified received electrical signal to obtain the real information back and give it to the concerned destination.

The received signal  $Y$  is the output of an integrate-and-dump filter which integrates the  $h \times x(t)$  over the symbol interval. This is processed by a detector whose aim is to determine the received data symbols. In our analysis it is assumed that the channel matrix  $H$  is known at the receiver. Moreover, the elements of  $N$  are taken to be independent but not identically distributed (i.i.d.) Gaussian random variables with mean 0 and variance  $\sigma_n^2$ , since the shot noise depends on the received signal.

Most advantages and abilities of MIMO systems come at a price vs. detection complexity. As in any communication system, the ideal receiver jointly detects and decodes the received signal vectors. There are many reduced complexity algorithms that have been proposed in order to solve the MIMO demodulation problem [12]. The simplest of these linear detectors is the zero forcing (ZF) detector, which simply calculates the inverse of the channel matrix. However, this can introduce significant noise enhancement and performance loss at low SNR. A somewhat more advanced equalizer is the minimum mean-squared error (MMSE) receiver, which takes into account the signal SNR while calculating the channel inverse. The ML demodulator is the optimal demodulator that finds the most likely transmitted vector based on the received signal. The channel matrix remains multidimensional, which



means we keep all the inter-stream interferences during the demodulation.

### 3.4.1 Decision Algorithm for the SISO Case

The decoder has a decision circuit that compares the sampled value of the current generated from the photodetector,  $I_p$ , as given by (3.4), with a threshold value  $I_d$  and calls it bit 1 if  $I_p > I_d$  or bit 0 if  $I_p < I_d$ . An error occurs if  $I_p < I_d$  for bit 1 because of receiver noise. An error also occurs if  $I_p > I_d$  for bit 0. Both sources of errors can be included by defining the error probability as

$$BER = p(1)P(0|1) + p(0)P(1|0). \quad (3.11)$$

where  $p(1)$  and  $p(0)$  are the probabilities of transmitting bits 1 and 0, respectively,  $P(0|1)$  is the probability of deciding 0 when 1 is transmitted, and  $P(1|0)$  is the probability of deciding 1 when 0 is transmitted. Assuming that for each receiver, 1 and 0 bits are equally likely to occur,  $p(1) = p(0) = 1/2$ , and the BER becomes

$$BER = 1/2[P(0|1) + P(1|0)]. \quad (3.12)$$

Only when the output of the detector exceeds the set threshold value do we say a pulse is present. False alarms occur when the noise alone exceeds the threshold value and is interpreted as the presence of a signal. On the other hand, if the signal plus noise does not exceed the threshold, it is called

a missed detection. Threshold detection concepts are illustrated in Fig. 3.4.

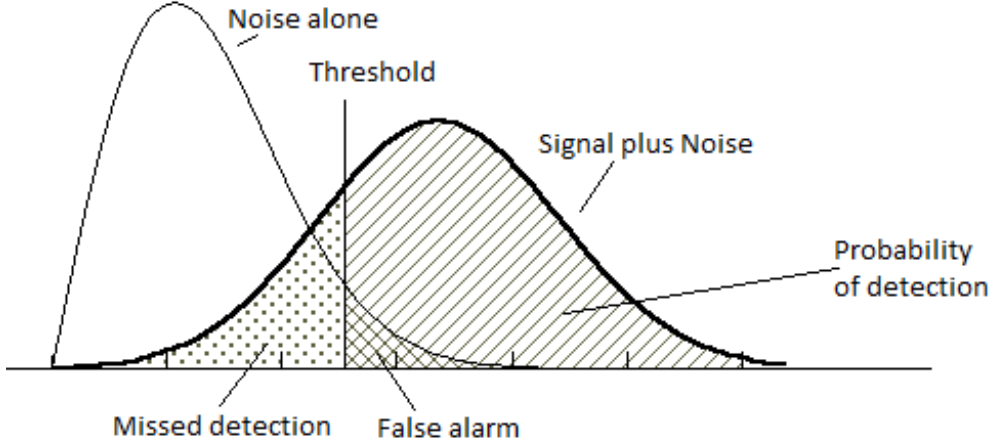


Figure 3.4: Probability of detection and false alarm.

Define  $\sigma_1^2$  and  $\sigma_0^2$  as noise variances, and  $I_1$ ,  $I_0$  as average currents, corresponding to a 1 and 0 bits received respectively. Thus,  $\sigma_1^2 = \sigma_n^2 \Big|_{1 \text{ transmitted}}$  and  $\sigma_0^2 = \sigma_n^2 \Big|_{0 \text{ transmitted}}$ . The conditional probabilities, as discussed in (3.12) corresponding to a decision threshold,  $I_d$ , are given by

$$P(0|1) = \frac{1}{\sigma_1 \sqrt{2\pi}} \int_{-\infty}^{I_d} \exp\left(-\frac{I - I_1^2}{2\sigma_1^2}\right) dI = \frac{1}{2} \left( \operatorname{erfc}\left(\frac{I_1 - I_d}{\sigma_1 \sqrt{2}}\right) \right). \quad (3.13)$$

$$P(1|0) = \frac{1}{\sigma_0 \sqrt{2\pi}} \int_{I_d}^{+\infty} \exp\left(-\frac{I - I_0^2}{2\sigma_0^2}\right) dI = \frac{1}{2} \left( \operatorname{erfc}\left(\frac{I_d - I_0}{\sigma_0 \sqrt{2}}\right) \right). \quad (3.14)$$

where  $\operatorname{erfc}$  stands for the complimentary error function.

Thus, the BER is now given by

$$BER = \frac{1}{4} \left[ \text{erfc}\left(\frac{I_1 - I_d}{\sigma_1 \sqrt{2}}\right) + \text{erfc}\left(\frac{I_d - I_0}{\sigma_0 \sqrt{2}}\right) \right]. \quad (3.15)$$

(3.15) shows that the BER depends on the decision threshold  $I_d$ . In practice,  $I_d$  is optimized to minimize the BER. Thus,  $I_d$  is chosen in such a way that it satisfies the following condition,

$$\begin{aligned} \frac{d}{dI_d} \left( \frac{1}{4} \left[ \text{erfc}\left(\frac{I_1 - I_d}{\sigma_1 \sqrt{2}}\right) + \text{erfc}\left(\frac{I_d - I_0}{\sigma_0 \sqrt{2}}\right) \right] \right) &= 0. \\ \implies \frac{(I_d - I_0)^2}{2\sigma_0^2} &= \frac{(I_d - I_1)^2}{2\sigma_1^2} + \ln\left(\frac{\sigma_1}{\sigma_0}\right) \end{aligned} \quad (3.16)$$

(3.17)

Using (3.17), the BER of the optimum ML receiver for the SISO case can be approximated as

$$BER = \frac{1}{2} \text{erfc}\left(\frac{Q}{\sqrt{2}}\right) \quad (3.18)$$

where  $Q = \frac{I_1 - I_0}{\sigma_1 + \sigma_0}$  when, from (3.17),  $I_d \approx \frac{\sigma_0 I_1 - \sigma_1 I_0}{\sigma_1 + \sigma_0}$  and  $\sigma_1 \approx \sigma_0$ .

### 3.4.2 Decoder Design for 2X2 MIMO Case Using a Decision Threshold

For a 2X2 MIMO case, each receiver receives a signal component from the corresponding transmitter and an interference component from the other

transmitter. Thus, the noise probability density function at the receiver depends on the data transmitted from both the transmitters.

Let  $P(x_1|x_1x_2)$ ,  $x_1, x_2 \in \{0, 1\}$ , denote the probability of deciding  $x_1$  when  $x_1$  is sent from the corresponding transmitter, and  $x_2$  is transmitted from the other transmitter.  $p(x_1x_2)$  denotes the probability that  $x_1$  and  $x_2$  is transmitted from the two transmitters respectively. The error probability at receiver 1, is now given by

$$BER_{MIMO} = p(00)P(1|00) + p(01)P(1|01) + p(10)P(0|10) + p(11)P(0|11). \quad (3.19)$$

Again, assuming that for each receiver 1 and 0 bits are equally likely to occur,  $p(11) = p(00) = p(01) = p(10) = 1/4$ , and the error probability becomes

$$BER_{MIMO} = 1/4 [P(1|00) + P(1|01) + P(0|10) + P(0|11)]. \quad (3.20)$$

Similar to (3.15), if  $\sigma_{11}^2$ ,  $\sigma_{10}^2$ ,  $\sigma_{01}^2$  and  $\sigma_{00}^2$  are noise variances, and  $I_{11}$ ,  $I_{10}$ ,  $I_{01}$  and  $I_{00}$  are average currents, corresponding to 11, 10, 01 and 00 bits transmitted from the two transmitters, the error probability for a receiver using a decision threshold,  $I_d^{MIMO}$ , as discussed in (3.20) becomes

$$\begin{aligned} BER_{MIMO} = & \frac{1}{8} [(\text{erfc}(\frac{I_{11} - I_d^{MIMO}}{\sigma_{11}\sqrt{2}})) + \text{erfc}(\frac{I_{10} - I_d^{MIMO}}{\sigma_{10}\sqrt{2}})) \\ & + (\text{erfc}(\frac{I_d^{MIMO} - I_{00}}{\sigma_{00}\sqrt{2}})) + (\text{erfc}(\frac{I_d^{MIMO} - I_{01}}{\sigma_{01}\sqrt{2}}))] \end{aligned} \quad (3.21)$$

In order to minimize  $BER_{MIMO}$ ,  $I_d^{MIMO}$  is chosen such that,

$$\frac{d}{dI_d^{MIMO}} BER_{MIMO} = 0. \quad (3.22)$$

The equation above does not provide a closed form expression for  $I_d^{MIMO}$ , thus we calculate it numerically.

### 3.4.3 Zero forcing/Decorrelation Receiver

Zero forcing (ZF) detection is a simple and effective technique for retrieving multiple transmitted data streams at the receiver. The zero forcing detector applies the inverse of the channel to the received signal, to restore the signal before the channel. The name zero forcing corresponds to bringing down the interference to zero. To get the transmitted signal vector,  $X$ , we know that we need to find a matrix,  $W_{ZF}$ , which satisfies

$$W_{ZF}H = I. \quad (3.23)$$

The zero forcing (ZF) linear detector for meeting this constraint is given by,

$$W_{ZF} = (H^T H)^{-1} H^T. \quad (3.24)$$

When  $H$  is square and invertible,  $W_{ZF} = H^{-1}$ .

Thus, the decoded signal  $\tilde{Y}_{ZF}$  at the output of the zero forcing detector is

$$\tilde{Y}_{ZF} = W_{ZF}Y = X + W_{ZF}N. \quad (3.25)$$

The ZF/decorrelation detector acts to force substreams interfering the desired substream to be zero at the output, as its name suggests. As a result, it rejects the interference component of the received signal at the filter output. The signal power is not affected; however, the noise is increased due to the  $W_{ZF}N$  component, which contains the noise generated due to the transmitted signal and part of the noise component due to the other transmitter.

We denote the noise covariance by  $\Sigma_{ij}^{ZF} = E[W_{ZF}NN^TW_{ZF}^T]$  when bits  $i$  and  $j$  ( $i, j \in \{0, 1\}$ ) are transmitted from transmitters 1 and 2, respectively. This noise covariance is expressed as

$$\Sigma_{ij}^{ZF} = \begin{bmatrix} (\sigma 1_{ij}^{ZF})^2 & 0 \\ 0 & (\sigma 2_{ij}^{ZF})^2 \end{bmatrix} = W_{ZF} \begin{bmatrix} \sigma 1_{ij}^2 & 0 \\ 0 & \sigma 2_{ij}^2 \end{bmatrix} W_{ZF}^T \quad (3.26)$$

$\sigma 1_{ij}^2$  and  $\sigma 2_{ij}^2$  are noise variances at receivers 1 and 2.

Similar to (3.21), the BER for ZF receiver 1 is given by

$$\begin{aligned} BER_{ZF} &= \frac{1}{8} [(\text{erfc}(\frac{I_{11}^{ZF} - I_d^{ZF}}{\sigma 1_{11}^{ZF} \sqrt{2}})) + \text{erfc}(\frac{I_{10}^{ZF} - I_d^{ZF}}{\sigma 1_{10}^{ZF} \sqrt{2}})) \\ &+ (\text{erfc}(\frac{I_d^{ZF} - I_{00}^{ZF}}{\sigma 1_{00}^{ZF} \sqrt{2}})) + (\text{erfc}(\frac{I_d^{ZF} - I_{01}^{ZF}}{\sigma 1_{01}^{ZF} \sqrt{2}}))] \end{aligned} \quad (3.27)$$

for  $I_d^{ZF}$  such that  $\frac{d}{dI_d^{ZF}} BER_{ZF} = 0$ .  $I_{11}^{ZF}$ ,  $I_{10}^{ZF}$ ,  $I_{01}^{ZF}$  and  $I_{00}^{ZF}$  are average currents at ZF receiver 1, corresponding to a 11, 10, 01 and 00 bits transmitted from the two transmitters.

### 3.4.4 MMSE Receiver

The MMSE receiver minimizes  $E[|e|^2]$ , where  $e$  is the error signal, which is the filter output minus the transmitted signal. We focus on designing an MMSE receiver,  $W$ , acting on a zero mean signal, such that it minimizes the mean square error. Thus our filter  $W$  solves

$$\min_W E[E[((W(Y - E[Y]) - (X - E[X]))^2|X]] \quad (3.28)$$

For the 2X2 MIMO case, since  $X$  is a signal with mean  $1/2$  and the noise  $N$  has zero mean, the mean square error from (3.28) becomes

$$MSE = E[E[(WHX - \frac{1}{2}WH + WN - IN + \frac{I}{2})^2|X]] \quad (3.29)$$

where  $I$  is the identity matrix.

Thus,

$$MSE = E[E[((WH - I))(X - \frac{1}{2})(X - \frac{1}{2})^T(WH - I)^T + WNN^TW|X]]. \quad (3.30)$$

For the MIMO 2X2 case, since we can have only 4 combinations of transmit-

ted bits (either 1 or 0 for each transmitter), the MSE becomes

$$\begin{aligned}
MSE = & \frac{1}{4}Tr[(WH - I)(\begin{bmatrix} 0 \\ 0 \end{bmatrix} - \frac{1}{2})(\begin{bmatrix} 0 \\ 0 \end{bmatrix} - \frac{1}{2})^T(WH - I)^T + W\Sigma_{00}^N W^T \\
& + (WH - I)(\begin{bmatrix} 1 \\ 0 \end{bmatrix} - \frac{1}{2})(\begin{bmatrix} 1 \\ 0 \end{bmatrix} - \frac{1}{2})^T(WH - I)^T + W\Sigma_{10}^N W^T \\
& + (WH - I)(\begin{bmatrix} 0 \\ 1 \end{bmatrix} - \frac{1}{2})(\begin{bmatrix} 0 \\ 1 \end{bmatrix} - \frac{1}{2})^T(WH - I)^T + W\Sigma_{01}^N W^T \\
& + (WH - I)(\begin{bmatrix} 1 \\ 1 \end{bmatrix} - \frac{1}{2})(\begin{bmatrix} 1 \\ 1 \end{bmatrix} - \frac{1}{2})^T(WH - I)^T + W\Sigma_{11}^N W^T]. \quad (3.31)
\end{aligned}$$

where  $\Sigma_{ij}^N, i, j \in \{0, 1\}$  represents the noise covariance when bits  $i$  and  $j$  are transmitted from the 2 transmitters. This noise covariance is expressed as

$$\Sigma_{ij}^N = \begin{bmatrix} \sigma 1_{ij}^2 & 0 \\ 0 & \sigma 2_{ij}^2 \end{bmatrix} \quad (3.32)$$

$\sigma 1_{ij}^2$  and  $\sigma 2_{ij}^2$  are noise variances at receivers 1 and 2. The MSE is now given by

$$\begin{aligned}
MSE = & \frac{1}{4}Tr[(WH - I)\begin{bmatrix} 1 & 0 \\ 0 & 1 \end{bmatrix}(WH - I)^T \\
& + W\Sigma_{00}^N W^T + W\Sigma_{10}^N W^T + W\Sigma_{01}^N W^T + W\Sigma_{11}^N W^T]. \quad (3.33)
\end{aligned}$$

Using (3.28) and (3.33) we obtain the optimum MMSE receiver matrix,  $W$ ,

$$\min_W \left( \frac{1}{4}Tr[(WH - I)\begin{bmatrix} 1 & 0 \\ 0 & 1 \end{bmatrix}(WH - I)^T + W\Sigma_{00}^N W^T + W\Sigma_{10}^N W^T + W\Sigma_{01}^N W^T + W\Sigma_{11}^N W^T] \right)$$

Solving (3.34) we get a closed form expression for  $W$  that depends on  $I_{ij}$ ,

$\sigma 1_{ij}^2$  and  $\sigma 2_{ij}^2$  for  $i, j \in \{0, 1\}$ .



For the MMSE, the decoded signal  $\tilde{Y}_{MMSE}$  at the output of the receiver is given by

$$\tilde{Y}_{MMSE} = WY = WHX + WN. \quad (3.34)$$

(3.34) shows the signal component  $WHX$  and the noise component  $WN$ . The current at the MMSE receiver 1,  $I_{ij}^{MMSE}$ , is now dependent on the MMSE receiver matrix  $W$  and the interference signal. The noise covariance for the noise at the output of the MMSE is given by

$$\Sigma_{ij}^{MMSE} = \begin{bmatrix} (\sigma 1_{ij}^{MMSE})^2 & 0 \\ 0 & (\sigma 2_{ij}^{MMSE})^2 \end{bmatrix} = W \begin{bmatrix} \sigma 1_{ij}^2 & 0 \\ 0 & \sigma 2_{ij}^2 \end{bmatrix} W^T \quad (3.35)$$

Using (3.21), the BER for MMSE receiver 1 is given by

$$\begin{aligned} BER_{MMSE} = & \frac{1}{8} [(\text{erfc}(\frac{I_{11}^{MMSE} - I_d^{MMSE}}{\sigma 1_{11}^{MMSE} \sqrt{2}})) + \text{erfc}(\frac{I_{10}^{MMSE} - I_d^{MMSE}}{\sigma 1_{10}^{MMSE} \sqrt{2}})) \\ & + (\text{erfc}(\frac{I_d^{MMSE} - I_{00}^{MMSE}}{\sigma 1_{00}^{MMSE} \sqrt{2}})) + (\text{erfc}(\frac{I_d^{MMSE} - I_{01}^{MMSE}}{\sigma 1_{01}^{MMSE} \sqrt{2}}))] \end{aligned}$$

for  $I_d^{MMSE}$  such that  $\frac{d}{dI_d^{MMSE}} BER_{MMSE} = 0$ .  $I_{11}^{MMSE}$ ,  $I_{10}^{MMSE}$ ,  $I_{01}^{MMSE}$  and  $I_{00}^{MMSE}$  are average currents at MMSE receiver 1, corresponding to a 11, 10, 01 and 00 bits transmitted from the two transmitters.

### 3.4.5 One Shot ML Receiver

The principle of maximum likelihood estimation (MLE), originally developed by R.A. Fisher in the 1920s, states that the desired probability distribution

is the one that makes the observed data most likely. The receiver selects the most likely signal, from the information that it has available. This information is of two kinds, the received signal  $y_i$  at receiver  $i$ , which is an observation, and knowledge about the message source, which transmits  $x_i \in \{0, 1\}$ . Given a received symbol, maximum likelihood decoding picks the symbol  $x_i$  to maximize

$$\max_{x_i} L(y_i|x_i) = \max\{P(y_i|x_i = 0), P(y_i|x_i = 1)\} \quad (3.36)$$

It chooses the codeword that maximizes the probability that  $y$  was received, given that the codeword was sent. In the case when all codewords are equally likely to be sent, this scheme is equivalent to maximum-a-posteriori decoding of  $x_i$ . By means of Bayes rule, (3.36) may be written as

$$L(x_i|y_i) = \frac{P(y_i \text{ received} \mid x_i \text{ sent}) \times P(x_i \text{ sent})}{P(y_i \text{ received})} \quad (3.37)$$

The probability,  $P(y_i \text{ received} \mid x_i \text{ sent})$  is simply the probability that the noise,  $n_i = y_i - x_i$ , since the channel noise is additive; the  $y_i$  is observed and either  $x_i = 0$ , or  $x_i = 1$  is hypothesized.

For our 2X2 MIMO case, at each received instant, the receiver performs a joint decoding for both the transmitted bits. Thus, we calculate the four likelihood functions, corresponding to the four transmitted bit pairs, for each receiver input  $y_1$  and  $y_2$  from (3.9) as given by

$$\begin{aligned}
L(Y|x_1x_2) &= \frac{1}{\sqrt{2\pi}(\sigma 1_{x_1x_2})} e^{-(y_1 - (\mu 1_{x_1x_2}))^2 / (2(\sigma 1_{x_1x_2}^2))} \\
&\times \frac{1}{\sqrt{2\pi}(\sigma 2_{x_1x_2})} e^{-(y_2 - (\mu 2_{x_1x_2}))^2 / (2(\sigma 2_{x_1x_2}^2))} \quad (3.38)
\end{aligned}$$

where  $Y = [y_1 y_2]^T$ .  $\mu 1_{x_1x_2}$ ,  $\mu 2_{x_1x_2}$ ,  $\sigma 1_{x_1x_2}^2$  and  $\sigma 2_{x_1x_2}^2$  correspond to the noise means and variances at receiver 1 and 2 respectively due to a transmitted vector  $[x_1 x_2]^T$  from transmitters 1 and 2.

The receiver finds  $\max_{x_1x_2} [L(Y|x_1x_2)]$  and then decodes the corresponding  $x_1x_2$  as the most likely transmitted pair among  $\{11, 10, 01, 00\}$ . This decoding is done at every symbol duration, and thus a transmitted vector is decoded by one shot detection at every received instant.

The joint ML receiver makes an error when the likelihood of observing  $Y$  for the actual transmission  $x_1x_2$  is less than any other transmitted pair. The probability of correct detection for the joint ML receiver is given by

$$P_{correct} = p(00)L(00|00) + p(01)L(01|01) + p(10)L(10|10) + p(11)L(11|11). \quad (3.39)$$

We assume  $\{11, 10, 01, 00\}$  to be equally likely, and the probability of correct detection is now given by

$$P_{correct} = 1/4 \left( \sum_{i=0}^1 \sum_{j=0}^1 P \left( L(Y|x_i x_j) \geq \max_{a \neq i, b \neq j} L(Y|x_a x_b) \right) \right) \quad (3.40)$$

The bit error rate for the joint ML one shot detector is given by

$$BER_{MMSE} = 1 - P_{correct}. \quad (3.41)$$

### 3.5 Numerical Results

In this section, we present numerical results comparing the performance of the three receivers: the zero forcing receiver, the MMSE receiver and the ML receiver. These comparisons are shown for the 2X2 MIMO communication system with varying channel loss parameters and data rates. Most UV systems utilize a PMT as the main receiver unit. Although it has high multiplication gain ( $10^6$ ), large detection area (we use  $1.77 \text{ cm}^2$  for simulations), and low dark current (we assume it to be around 1 pA), it is fragile, bulky, and costly. It also requires a high voltage supply. These features definitely prevent low cost design. Currently, commercial solid state based photodiodes at the deep UV band are not available and research needs to be done in that area. The quantum efficiency of the PMT is taken to be 0.2.

The receiver performance for a NLOS UV link with no interference operating at 1 Mbps is depicted in Fig. 3.5.  $h_{11}$  is the path loss coefficient for the nondispersive channel, for channel 1, from transmitter 1 to receiver 1. In the geometry considered,  $\theta_1 = 20^\circ$ ,  $\theta_2 = 30^\circ$ ,  $\phi_1 = 17^\circ$ ,  $\phi_2 = 30^\circ$ , and  $r = 100$  m. Similarly,  $h_{22}$  is the impulse response path loss for channel 2, from trans-

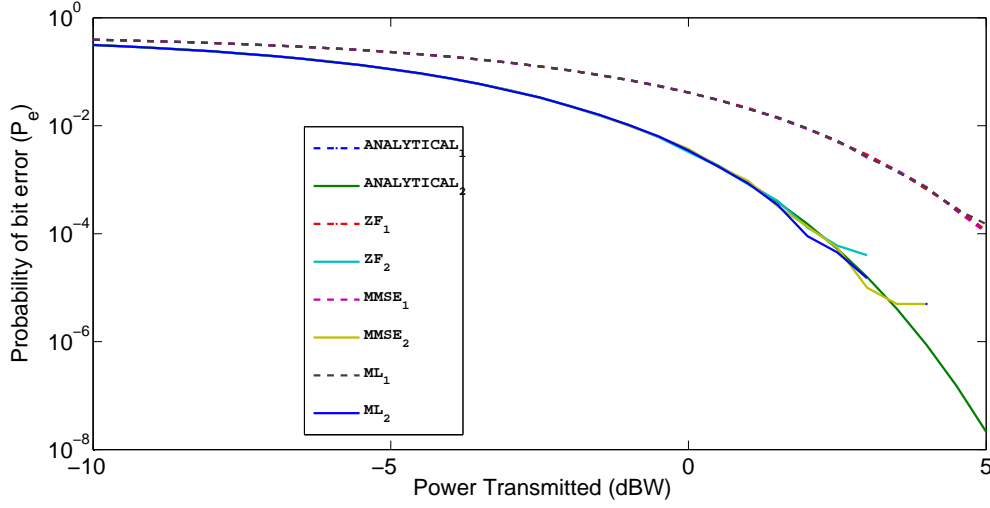


Figure 3.5: BER performance for  $h_{11} = -99.65$  dB,  $h_{12} = 0$ ,  $h_{21} = 0$  and  $h_{22} = -96.81$  dB. Simulated probability of error vs transmitted power is plotted for all three receivers and the analytical result from (3.18).

mitter 2 to receiver 2 for a geometry given by  $\theta_1 = 20^\circ$ ,  $\theta_2 = 25^\circ$ ,  $\phi_1 = 10^\circ$ ,  $\phi_2 = 40^\circ$ , and  $r = 100$  m. There is no overlap between the transmitter 1-receiver 2 beams and the transmitter 2-receiver 1 beams; thus,  $h_{12}$  and  $h_{21}$  are zero. Notice that all the three receivers give the same performance, which in turn overlaps with the analytical result derived in (3.18). Since this is a case with no co-channel interference, all the three receivers are optimal and give equal performance. Thus, for such a system we can implement a single user low complexity receiver, which gives us the same performance at the desired transmission rate. Notice that the curve for receiver 1 lies above the

receiver 2 BER curve, since the transmission loss due to channel 1 is nearly 3 dB higher than channel 2.

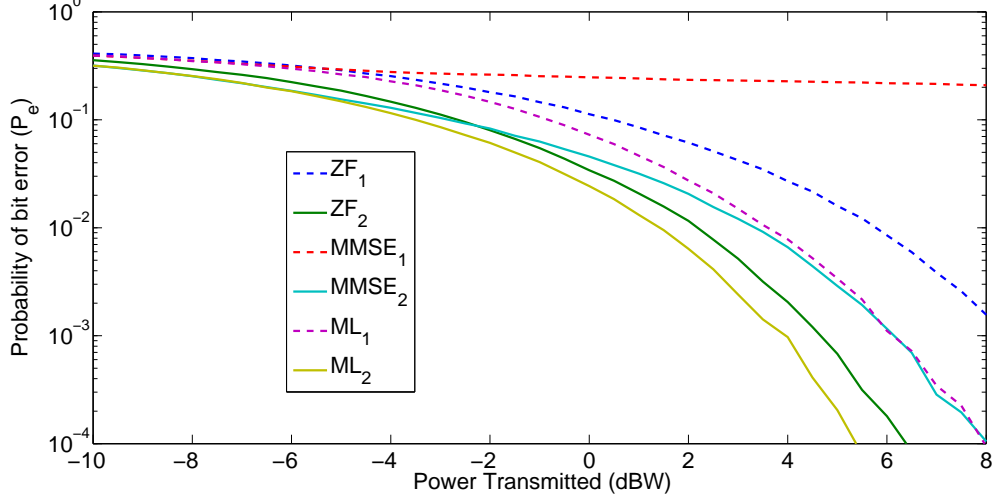


Figure 3.6: BER performance for  $h_{11} = -99.65$  dB,  $h_{12} = -102.66$  dB,  $h_{21} = -102.66$  dB and  $h_{22} = -96.81$  dB. Simulated probability of error vs transmitted power is plotted for all three receivers: ZF, MMSE and ML.

Fig. 3.6 depicts receiver performance for a NLOS UV link with significant interference operating at 1Mbps. Channels 1 and 2 have a geometry similar to the one considered in Fig. 3.5. In Fig. 3.6 channel 1 is affected more severely by interference from transmitter 2, which is nearly half the received signal. Channel 2 has a higher gain and is slightly more immune to interference from channel 1. We observe that, as predicted because of the joint likelihood decoding involved, the maximum likelihood decoder performs best for both the receivers. However the MMSE performs worse than the ZF

receiver for higher power levels, and specifically much worse in the case of receiver 1 due to higher signal interference. Since the zero forcing receiver decorrelates the incoming input streams at both the receivers, the output of the decorrelator from each receiver is just the corresponding transmitted vector affected by noise. The receiver rejects the interference component and hence, the resulting SNR at the output of the ZF receiver is high. A threshold applied to such an output results in good performance. In the case of the MMSE receiver, the receiver output still contains interference components. The sum of the transmitted signal with the interference component increases the power even more at higher transmitted power levels, thus contributing to more noise and lowering the threshold decoder performance. This can be understood better with signal maps.

The ideal constellation space for a system with no interference, shown in Fig. 3.7, provides proper decoding with the optimum threshold. However, in the case of significant interference at higher transmitter power levels, the constellation gets skewed as shown in Fig. 3.8.

Fig. 3.8 shows the case with significant interference from the adjacent channel. The threshold for signal 1 does not lead to optimum decoding anymore since the interference and noise components make both the constellation points for receiver 1 much closer and undistinguishable on average. Since the optical receiver used is shot noise limited, increasing interference from the

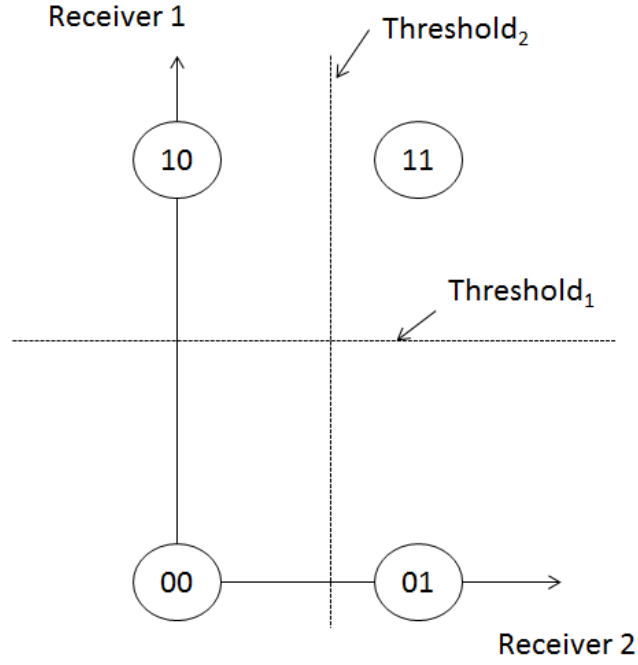


Figure 3.7: Ideal constellation corresponding to the NLOS UV link with no interference.

adjacent channel increases the effect of the noise further. For channel 1, this effect is significant because the interfering signal has comparable power levels with the actual signal. However, since channel 2 has a larger SINR, it can still be decoded correctly. Thus the MMSE detector performs worse in such a situation. The ZF receiver on the other hand converts the one in Fig. 3.8 to that in Fig. 3.7 and thus works better. The MMSE detector does perform better than the ZF receiver in cases of low interference and low transmit power, and hence on average, tends to perform well. However, for extreme



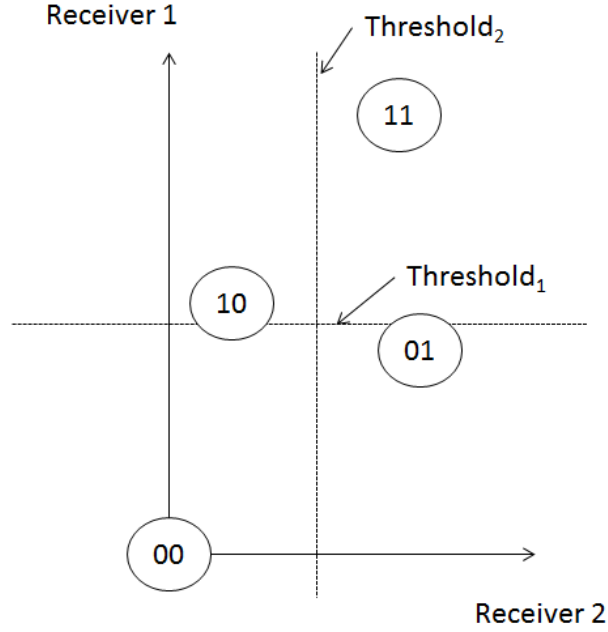


Figure 3.8: Constellation corresponding to the NLOS UV link with severe interference.

cases of high interference, it fails.

### 3.6 Chapter Summary

In this chapter, receiver design techniques are considered for cases where the channel is nondispersive for the 2X2 MIMO UV NLOS communication system. The performances of the three receivers designed: the zero forcing receiver, the minimum mean square error (MMSE) receiver and the maximum likelihood receiver (ML receiver) is simulated for a communication system.

All three receivers perform equally well on a MIMO system with no or negligible interference; a low complexity receiver can be used in such cases. i.e., a single user. The results obtained agree with the BER calculated analytically. In the case of high interference from the other channel, the more complex ML receiver outperforms the ZF and the simpler MMSE receivers, with the MMSE receiver showing the worst performance. Engineering tradeoffs can be considered before choosing the right receiver in such cases.

# Chapter 4

## Receiver Design for ISI Case

In the previous chapters, we considered the zero forcing, minimum mean square error, and the maximum likelihood detectors. All these equalizers concentrate on reducing the probability of error for each bit in the receiver output. However, when the signal experiences dispersion, what we really want to do is minimize the probability that the receiver chooses the wrong sequence of bits as its output, that is, with a given received vector, we want to maximize the probability that a particular sequence of bits was transmitted. The brute-force maximum-likelihood receiver achieves the minimum word error probability, but generally is far too complicated to implement in almost all cases of interest. If an  $n$ -bit sequence is transmitted, then there are  $2^n$  likelihoods to be computed before the largest likelihood can be determined, and the computational task is overwhelming except in the uninteresting case

of small  $n$ .

Interestingly enough, for transmission over band-limited channels, there exists a clever re-formulation of the computational task that allows the receiver to determine the largest likelihood without computing all  $2^n$  likelihoods. This is achieved by computing likelihoods iteratively as each symbol is received, and discarding all those (partial) likelihoods which are small enough for us to be sure that they never going to grow large enough to be the maximum likelihood when the processing is complete. Such tree pruning reduces the computational burden, and makes maximum-likelihood sequence estimators feasible. Indeed, the limiting factor is not  $n$ , the number of bits transmitted, but the length of the channel response  $h[\cdot]$ . The complexity of the maximum-likelihood sequence estimator grows exponentially with the channel response length, and at best linearly with  $n$  [15]. In order to save design and time complexity, another approach is the maximum a-posteriori probability algorithm that makes decisions on a symbol-by-symbol basis, but each symbol decision is based on an observation of a short sequence of received signal vectors. Both detectors require prior information about the channel and hence information about ISI.

## 4.1 ISI Model of the Channel

When the channel transfer function varies significantly over the frequency band of interest, the effect of the channel on the transmitted signal needs to be taken into account. Such channels are called frequency selective or bandwidth-limited channels, and they cause a phenomenon called intersymbol interference. As the name implies, intersymbol interference (ISI) means that each sample value in the receiver depends not just on the symbol being demodulated but also on the other symbols being transmitted.

The transmitted signal  $x(t)$  is given by

$$x(t) = \sum_i x_i p_T(t - iT) \quad (4.1)$$

where  $x_i \in \{0, 1\}$  and  $p_T(t)$  is the transmitted signal pulse shape, assumed to have a band-limited frequency response.

This transmitted signal  $x(t)$  passes through the NLOS scattering channel and then the receive filter whose responses are denoted by  $h_{ch}(t)$  and  $h_R(t)$ , respectively. The received signal  $y(t)$  is given by

$$y(t) = x(t) * h_{ch}(t) * h_R(t) + n(t) * h_R(t) \quad (4.2)$$

where  $n(t)$  is the receiver noise as discussed earlier. This is the noise generated at the receiver due to shot noise and thermal noise components. The equivalent transmitted pulse, channel, and receiver response,  $h_e(t)$ , can be

shown as

$$h_e(t) = p_T(t) * h_{ch}(t) * h_R(t) \quad (4.3)$$

In order to process the continuous time received signal,  $y(t)$ , in discrete time, it is sampled at every bit interval,  $T$  as in the following equations.

$$\begin{aligned} y(mT) &= y(t) \Big|_{t=mT} \\ y[m] &= \sum_i x_i * h_e(mT - iT) + n(mT) \end{aligned} \quad (4.4)$$

with,

$$\begin{aligned} h_e[j] &= h_e(jT) \\ n[m] &= n(mT) \end{aligned} \quad (4.5)$$

Since  $T$  is the reciprocal of the receiver filter bandwidth, the noise samples remain independent. (4.4) now becomes

$$y[m] = \sum_j h_e[j] x_{m-j} + n[m] \quad (4.6)$$

The sampling time is chosen such that the received signal  $y[m]$  has the highest power from the corresponding signal  $x[m]$  and not the adjacent signals. This translates to selecting a sampling time from the eye pattern obtained on the basis of the channel dispersion. The sampling time provides the maximum signal to noise power ratio for a given transmitted symbol waveform. The process of generating the sampled channel coefficients is explained in further

detail in the next section. Thus, the  $m$ -th sample contains the largest contribution from  $x[m]$  together with contributions from past signals  $x[m-1]$ ,  $x[m-2]$ ,  $\dots$ , etc., and also from the future signals  $x[m+1]$ ,  $x[m+2]$ ,  $\dots$ , etc..

Obviously, a brute force approach to the problem of MLSE is to enumerate all permissible source sequences, which requires  $2^n$  calculations. To derive a more efficient algorithm, we note that the channel can be described using a state diagram, i.e., by a finite-state machine. For example, an OOK system with channel impulse response  $h = (h[0], h[1]) = (1, 0.5)$  has the state diagram as shown in Fig. 4.1(a). Alternatively, it can be represented by a two-state trellis diagram. Fig. 4.1(b) shows all possible transitions of states over time. Note that state  $s_i$  is defined as  $(x_{i-1})$  and each transition  $(s_i, s_{i+1})$  is associated with an expected observation  $y(s_i, s_{i+1}) = h_0 x_i + h_1 x_{i-1}$ .

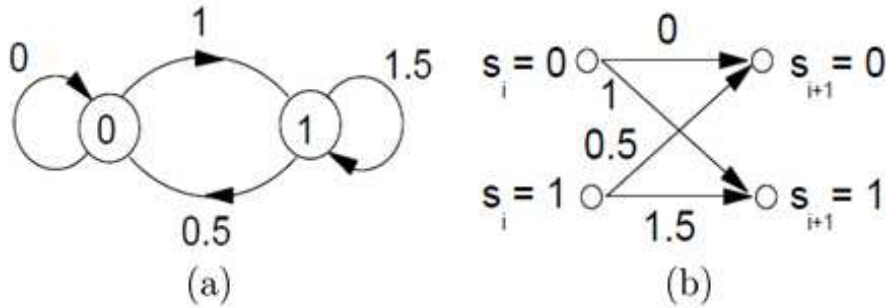


Figure 4.1: (a) State diagram of the channel  $h = (1, 0.5)$  for binary transmission. (b) One stage of the corresponding two-state trellis.

## 4.2 Communication System and Impulse Response Coefficient Description

As shown in Fig. 3.3, a typical NLOS UV communication system generally includes three subsystems— the transmitter, the receiver and the atmospheric optical channel. At the transmitter, electronic signals being conveyed need to be coded and modulated, then fed to the source driver, which controls the UV source to emit UV light. Here, the system adopts an internal modulating method; of course, the system could instead use an external modulation. UV light with some emitting cone is scattered by atmospheric components such as molecules, aerosol and particles. This kind of scattering is the main mechanism forming multiple paths to convey information, being collected by the wide field of view of receivers. Scattered light is focused on a photodetector by an optical system. However, received signal intensity is weak due to absorption and scattering in the free space channel. Therefore, signals need to be amplified through a preamplifier. An integrate-and-dump filter is used to accumulate the received signal. Since we assume on-off keying modulation, the optimum filter from the point of view of signal detection is one matched to the received pulse. Since the received pulse-shape depends on the channel response, the receiver cannot be easily designed to match it. Instead, the receiver input is convolved with a rectangular pulse of duration  $T$  seconds



(the symbol duration). This means that the followed by integrating the pulse and then sampling it at  $T$  sec. The accumulator is reset, and the integration and sampling is repeated.

Fig. 3.3 shows the general principle of UV communications. The detector block contains the trellis decoder, i.e., the maximum likelihood sequence estimator (MLSE) to provide the most likely sequence of transmitted bits or the maximum-a-posteriori (MAP) detector which has prior information about the ISI.

When the received signal has no memory, i.e., for a nondispersive channel, the symbol-by-symbol ML detector described in the preceding chapter is optimal. When the received signal has memory due to the channel, i.e., signals received in successive symbol intervals are dependent on signals transmitted previously, the MLSE detector is suitable because it bases its decisions on observation of a sequence of received signals over successive signal intervals.

We observed in Chapter II that for distances up to 100 m and low transmit receive angles, channel losses are acceptable for voice communications. Channel delay spread causes ISI, which, unless equalization is used, causes an irreducible error floor, hence limiting maximum data rate. Specifically, if the symbol period of baseband data pulse is larger than that of delay spread, ISI will be generated at the receiver. That is, the data signals on two neighboring pulse periods overlap, which causes the receiver not to be

able to distinguish them. Mitigation of ISI is required when the modulation symbol time is of the order of the channel's rms delay spread. For our case, we assume maximum rates of up to 3 Mbps since the channel delay spread is of the order of a micro second for a system with geometry  $\theta_1 = 85^\circ$ ,  $\theta_2 = 85^\circ$ ,  $\phi_1 = 40^\circ$ ,  $\phi_2 = 90^\circ$  and  $d = 20$  m, as seen from Fig. 4.2. The eye diagram

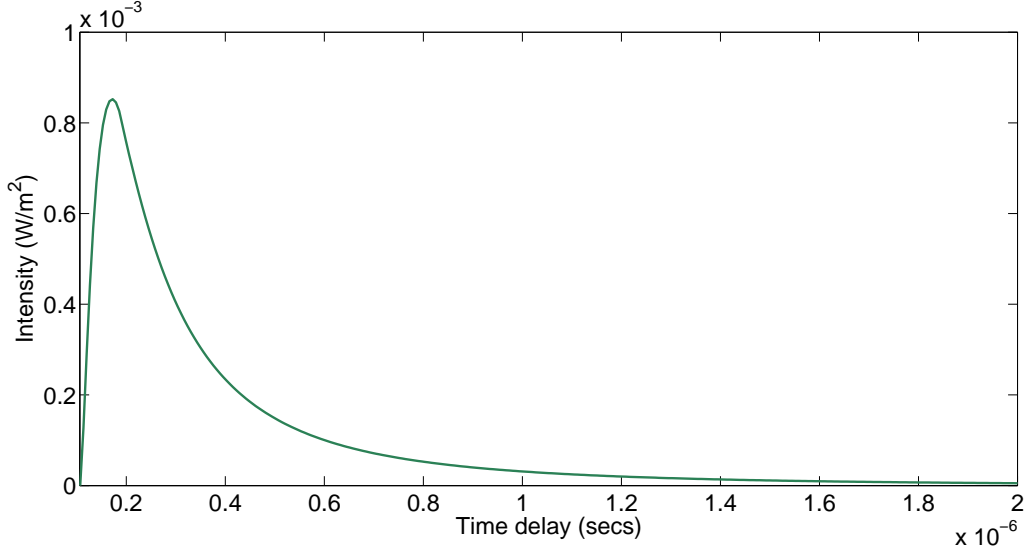


Figure 4.2: Impulse response for UV NLOS communication link with  $\theta_1 = 85^\circ$ ,  $\theta_2 = 85^\circ$ ,  $\phi_1 = 40^\circ$ ,  $\phi_2 = 90^\circ$  and  $d = 20$  m.

depicting the ISI effect of such a single channel on an OOK transmission is depicted in Fig. 4.3

The design of the appropriate MLSE receiver for the 2X2 MIMO UV NLOS channel depends on the communication data rate and the system geometry. For designing a practical trellis decoder, we consider a memory of

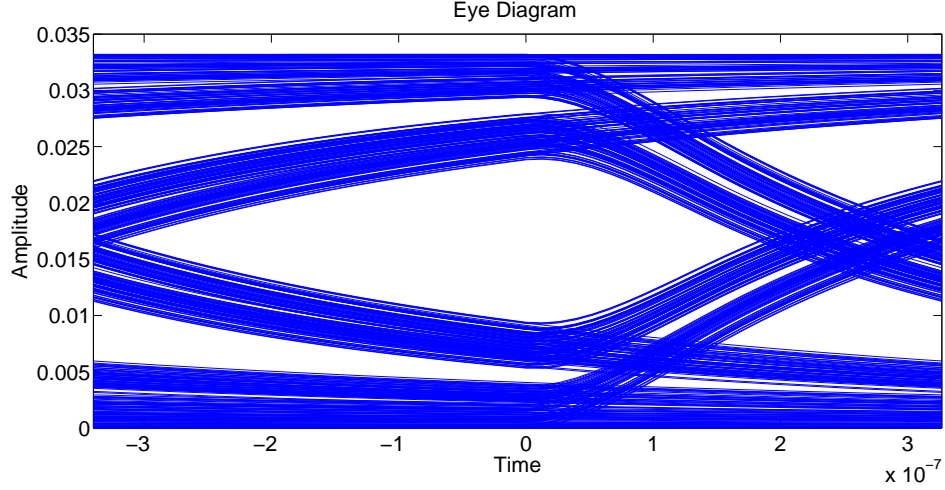


Figure 4.3: Eye pattern for a UV NLOS communication link with  $\theta_1 = 85^\circ$ ,  $\theta_2 = 85^\circ$ ,  $\phi_1 = 40^\circ$ ,  $\phi_2 = 90^\circ$  and  $d = 20$  m operating at 3 Mbps.

one or two symbols, and thus the power delay spread should be modelled with the right channel impulse response coefficients. This is done by the integrate-and-dump filter, which integrates the spread received pulse over the symbol duration so as to maximize the path loss to the current transmitted bit. This is shown for a channel with two symbols of memory in Fig. 4.4. Similarly, to model a channel with a memory of one symbol,  $h[0]$  is retained. The other larger loss coefficient ( $\max(h[-1], h[1])$ ) is considered as the ISI component for the adjacent transmitted bit for the same channel. In order to design a receiver, ISI contributions from the same channel as well as the interference from ISI due to the adjacent channel must be considered at each receiver to calculate the received signal distributions.

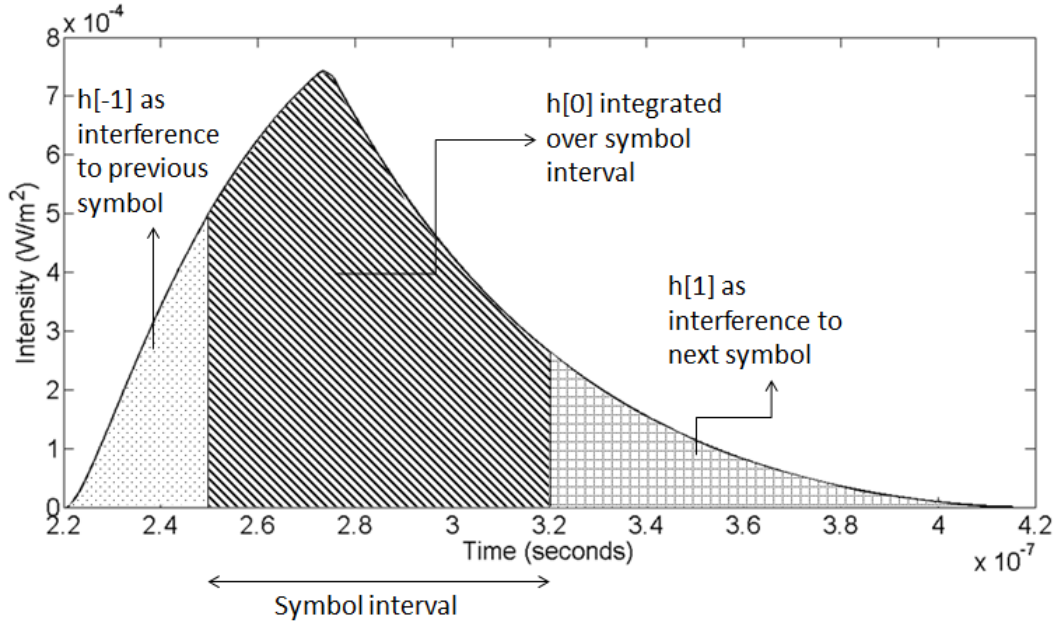


Figure 4.4: Impulse response coefficients for channel with memory 2.

For a UV NLOS system with  $\theta_1 = 85^\circ$ ,  $\theta_2 = 85^\circ$ ,  $\phi_1 = 40^\circ$ ,  $\phi_2 = 90^\circ$  and  $d = 20$  m operating at 3 Mbps, the channel can be described by coefficients  $(h[-1], h[0], h[1]) = 10^{-9} \times (0.0139, 0.1124, 0.0655)$ . If the same system operates at 2 Mbps, we observe lower ISI and the channel can be described by  $(h[0], \max(h[-1], h[1])) = 10^{-9} \times (0.1124, 0.0655)$ .

### 4.3 MAP Receiver Design

As discussed in Chapter 3, For our 2X2 MIMO case, at each received instant, the receiver performs a joint decoding for both the transmitted bits. The maximum-a-posteriori detector for this case can be described as

$$\begin{pmatrix} \tilde{x}_1 \\ \tilde{x}_2 \end{pmatrix} = \max P \left( \begin{pmatrix} x_1 \\ x_2 \end{pmatrix} \middle| \begin{pmatrix} y_1 \\ y_2 \end{pmatrix} \right) \quad (4.7)$$

where  $\begin{pmatrix} \tilde{x}_1 \\ \tilde{x}_2 \end{pmatrix}$  is the output of the MAP receiver.

Thus, we calculate the likelihood functions, corresponding to the 4 transmitted bit pairs (00, 01, 10, 11), for each receiver input  $y_1$  and  $y_2$  from (3.9).

The likelihood function is given by

$$\begin{aligned} P(Y|x_1x_2) &= \frac{1}{\sqrt{2\pi}(\sigma 1_{x_1x_2})} e^{-(y_1 - (\mu 1_{x_1x_2}))^2 / (2(\sigma 1_{x_1x_2})^2)} \\ &\times \frac{1}{\sqrt{2\pi}(\sigma 2_{x_1x_2})} e^{-(y_2 - (\mu 2_{x_1x_2}))^2 / (2(\sigma 2_{x_1x_2})^2)} \end{aligned} \quad (4.8)$$

where  $\mu 1_{x_1x_2}$ ,  $\mu 2_{x_1x_2}$ ,  $\sigma 1_{x_1x_2}^2$  and  $\sigma 2_{x_1x_2}^2$  correspond to the signal means and noise variances at receiver 1 and 2 respectively, due to a transmitted vector  $x_1x_2$  from transmitters 1 and 2.

If the receiver has prior knowledge about the ISI due to the channel, it can calculate a more accurate likelihood function based on this prior knowledge. Thus, at each received instant, the receiver calculates all likelihoods corresponding to ISI possibilities from bits sent in the previous interval. For a channel with a memory of two symbols, it calculates 8 cases ( $2^3$ , for the current bit and two adjacent bits sent) for each transmitter and calculates 64 likelihood functions in total for the joint decoding case. For such a channel with a memory of two symbols, we denote the vector  $\mathbf{x}_1$  to correspond to

the possible  $(x_1^{[-1]}, x_1^{[0]}, x_1^{[1]})$  series of symbols transmitted from transmitter 1, with  $x_1^{[0]}$  being the current symbol transmitted and  $(x_1^{[-1]}, x_1^{[1]})$  referring to the 2 adjacent symbols. Similarly, for the case with one symbol of ISI or channel impulse response corresponding to a memory of one, the vector  $\mathbf{x}_1$  corresponds to  $(x_1^{[-1]}, x_1^{[0]})$  series of possible symbols transmitted from transmitter 1. For the received vector  $Y = [y_1 y_2]^T$ , the MAP receiver hypothesizes that  $[x_1^{[0]} x_2^{[0]}]^T$  was sent and calculates the most likely transmitted vector by taking into account ISI contributions from all possible adjacent bit patterns. This MAP receiver is given by

$$\max_{x_1^{[0]}, x_2^{[0]}} \sum_{x_1^{[-1]}, x_1^{[1]}, x_2^{[-1]}, x_2^{[1]}} P(Y|\mathbf{x}_1 \mathbf{x}_2) P(\mathbf{x}_1 \mathbf{x}_2). \quad (4.9)$$

Each likelihood function is calculated as

$$\begin{aligned} P(Y|\mathbf{x}_1 \mathbf{x}_2) &= \frac{1}{\sqrt{2\pi}(\sigma 1_{\mathbf{x}_1 \mathbf{x}_2})} e^{-(y_1 - (\mu 1_{\mathbf{x}_1 \mathbf{x}_2}))^2 / (2(\sigma 1_{\mathbf{x}_1 \mathbf{x}_2}^2))} \\ &\times \frac{1}{\sqrt{2\pi}(\sigma 2_{\mathbf{x}_1 \mathbf{x}_2})} e^{-(y_2 - (\mu 2_{\mathbf{x}_1 \mathbf{x}_2}))^2 / (2(\sigma 2_{\mathbf{x}_1 \mathbf{x}_2}^2))} \end{aligned} \quad (4.10)$$

where  $\mu 1_{\mathbf{x}_1 \mathbf{x}_2}, \mu 2_{\mathbf{x}_1 \mathbf{x}_2}, \sigma 1_{\mathbf{x}_1 \mathbf{x}_2}^2$  and  $\sigma 2_{\mathbf{x}_1 \mathbf{x}_2}^2$  correspond to the signal means and variances at receiver 1 and 2 respectively, due to the possible transmitted vector  $\mathbf{x}_1 \mathbf{x}_2$  from transmitters 1 and 2. To calculate  $P(\mathbf{x}_1 \mathbf{x}_2)$ , we assume that all symbols are independent and equally likely to be sent.

For a channel with a memory of two symbols, we denote the vector  $\mathbf{h}$  as the channel impulse response with coefficients  $(h[-2], h[0], h[1])$ . For the

2X2 system described in Fig. 3.2, the ISI channel responses are now given by  $\mathbf{h}_{11}$ ,  $\mathbf{h}_{12}$ ,  $\mathbf{h}_{21}$  and  $\mathbf{h}_{22}$ . The signal means at the receiver, are calculated as

$$\begin{aligned}\mu_{1\mathbf{x}_1\mathbf{x}_2} &= \mathbf{h}_{11} * \mathbf{x}_1 + \mathbf{h}_{21} * \mathbf{x}_2 \\ \mu_{2\mathbf{x}_1\mathbf{x}_2} &= \mathbf{h}_{22} * \mathbf{x}_2 + \mathbf{h}_{12} * \mathbf{x}_1\end{aligned}\quad (4.11)$$

The corresponding noise variances can be obtained using (3.4), (3.6) and (3.7). The noise variance for receiver 1 is given by

$$\begin{aligned}I_p^{(1)} &= \Re GP_t(\mu_{1\mathbf{x}_1\mathbf{x}_2}) \\ \sigma_{1\mathbf{x}_1\mathbf{x}_2}^2 &= 2qG^2(I_p^{(1)} + I_d)\Delta f + \left(\frac{4kT_p}{R_{load}}\right)F_n\Delta f\end{aligned}\quad (4.12)$$

The noise variance for receiver 2 can be obtained similarly.

## 4.4 MLSE Receiver Design

Recall that in our model, the data being transmitted by each beam is a sequence  $x_i$  of independent random variables taking on equally likely values  $\{1, 0\}$ , and the channel output can be expressed as a sequence  $y[m]$  where

$$y[m] = \sum_j h_e[j]x_{m-j} + n[m] \quad (4.13)$$

As discussed in Fig. 4.1, we define the state,  $s_k$ , of an  $L$  tap channel as

$$s_k = x[k-1], x[k-2], \dots, x[k-L] \quad (4.14)$$

The new state is a combination of the new bit and  $(L - 2)$  bits from the state  $s_k$  as,

$$s_{k+1} = x[k], x[k - 1], x[k - 2], \dots, x[k - L + 1]. \quad (4.15)$$

The maximum likelihood sequence estimation (MLSE) becomes a problem of finding the sequence with the maximum likelihood as shown in

$$\max_{\text{all sequences of } x_k} P(y_1, y_2, \dots, y_n | x_1, x_2, \dots, x_n). \quad (4.16)$$

Thus, it is possible to describe the computations of the likelihoods as traversing the edges of a trellis, which is shown in Fig. 4.5. In a trellis, each intersection point (node) corresponds to a distinct state at a given time, and each line represents a transition to some new state at the next instant of time. The trellis begins and ends at known states, in our case the 00 transmitted symbol from the two transmitters. It is most important in decoding that every possible state sequence corresponds to a unique path through the trellis, and vice versa.

The decoder has to find the bit sequence that generates the state sequence “nearest” to the received sequence  $y_k$  in a probabilistic sense. Each transition in the trellis depends only on the starting state and the ending state. We know what would be the output from a state (without noise) would be, and



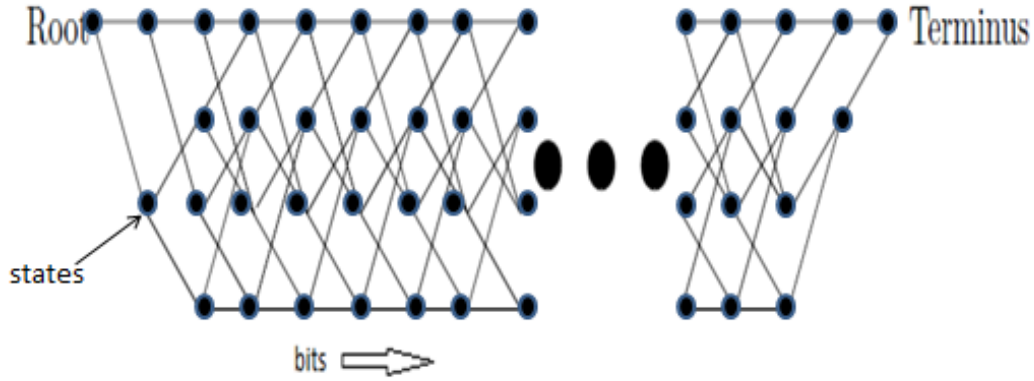


Figure 4.5: A sample trellis.

this noiseless state output gives the mean value for the observation  $y_k$ . The total probability for a state sequence is the sum of all the log-likelihoods along the path of the state sequence in the Markov chain. The Viterbi algorithm works in the following manner:

1. For all transitions in the trellis compute the sum of the likelihood in the initial state and in the transition

$$L(s_0, s_1, \dots, s_{k+1}) = \sum_{j=1}^k L(s_j | s_{j-1}) + L(s_0). \quad (4.17)$$

2. As shown in Fig. 4.6, at each state, select among the incoming paths the one with the maximum likelihood (the survival)

$$L(s_{k+1}) = \max L(y_k | s_k, s_{k+1}). \quad (4.18)$$

3. At each state, remember the previous surviving state (in previous stage) and the bit corresponding to the surviving path.

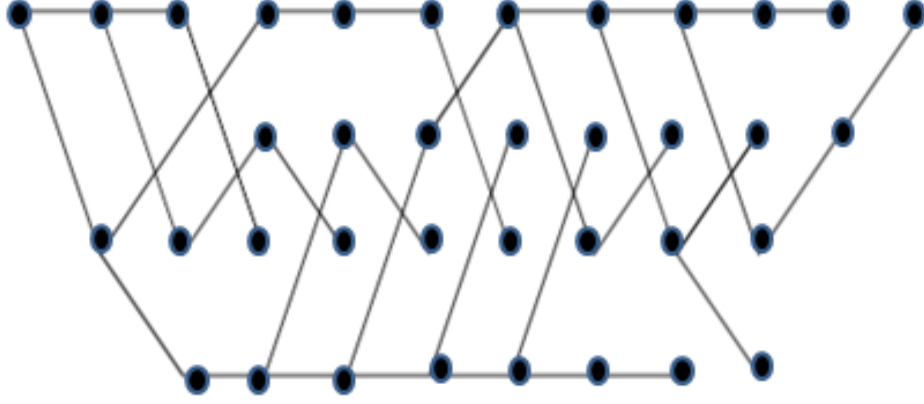


Figure 4.6: Example of progression of the Viterbi algorithm through the trellis.

The trellis for our 2X2 MIMO case for NLOS UV channels having a memory of one symbol is shown in Fig. 4.7. The states of the channel (circles) represent the previous received bit combination from receiver 1 (top bit) and receiver 2 (bottom bit). Each state now has 4 possible transitions to the next state, which correspond to the bit combination transmitted for the current received bits. The trellis starts at state  $\begin{bmatrix} 0 \\ 0 \end{bmatrix}$  and ends at the same state.

Similarly, for the 3 tap channel case, the ISI components affect two adjacent bits, i.e., the previous and the next bits, and the trellis for such decoding is as shown in Fig. 4.8. The 1 and 0 symbols represent “1” and “0” transmitted symbols, respectively. Each node is labeled with the previous two adjacent data symbols,  $x[m-2]$  and  $x[m-1]$ , for each transmitter (transmitter 1 stacked over transmitter 2). Due to lack of space, the branch labels

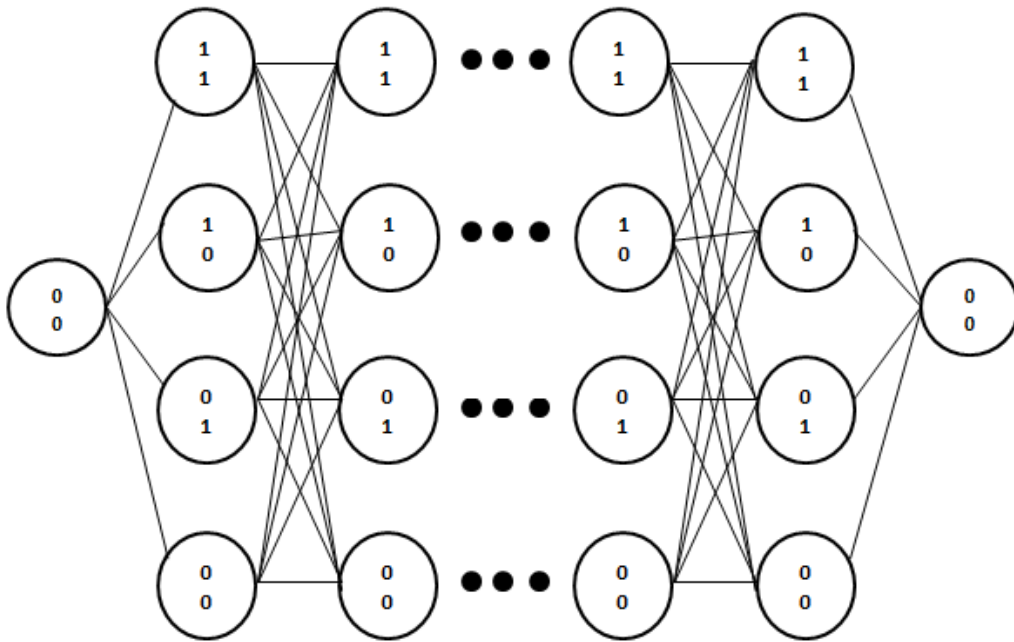


Figure 4.7: Trellis diagram for the 2 tap channel model of the 2X2 MIMO system.

are not shown on the figure but are calculated as shown in (4.17).

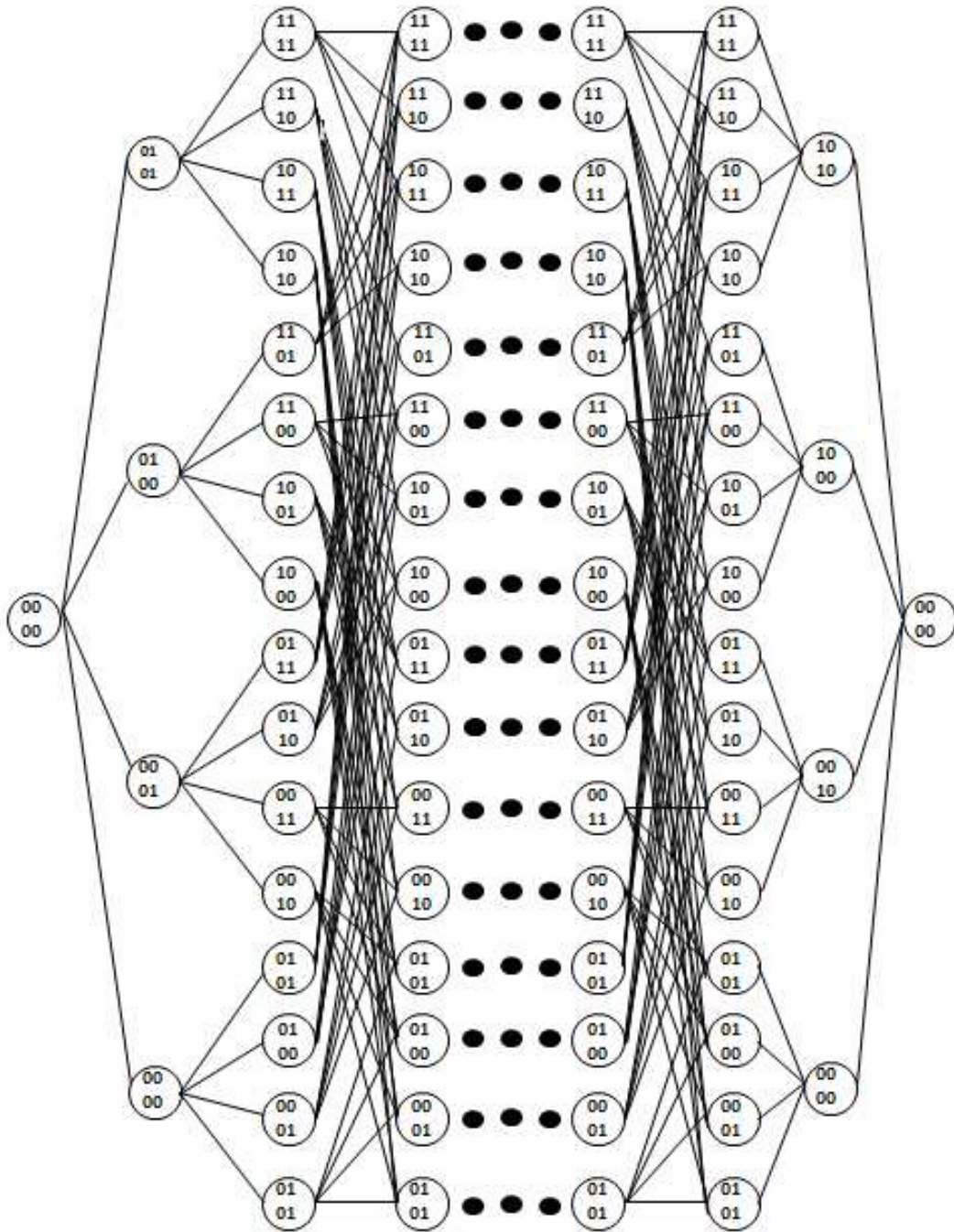


Figure 4.8: Trellis diagram for the 3 tap channel model of the 2X2 MIMO system.

## 4.5 Numerical Results

In this section we present numerical performance evaluation and simulation results for the NLOS UV system with a dispersive channel

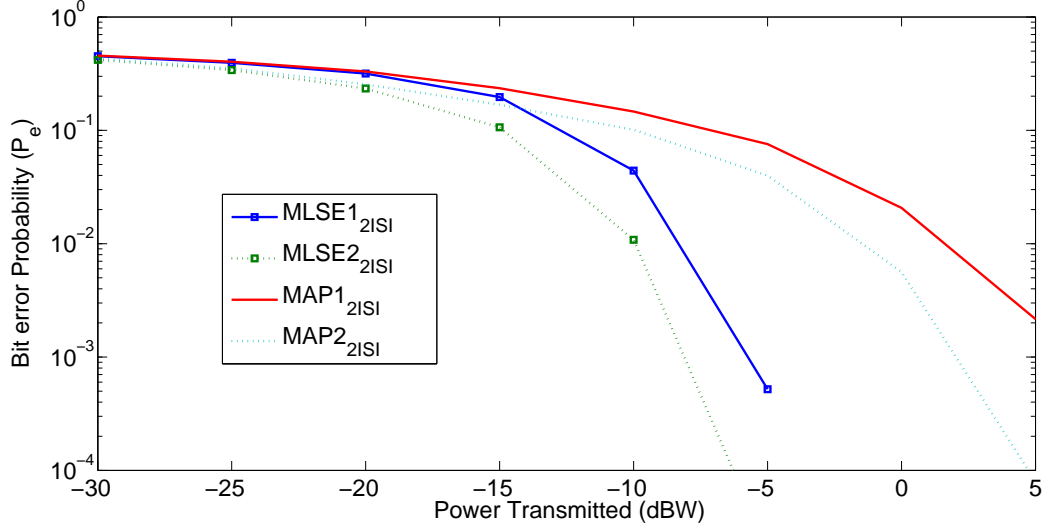


Figure 4.9: Receiver performance comparison for system operating at 3 Mbps and with geometry  $\theta_1 = 85^\circ$ ,  $\theta_2 = 85^\circ$ ,  $\phi_1 = 40^\circ$ ,  $\phi_2 = 90^\circ$  and  $d = 20$  m for both the transmitter-receiver pairs. Channel with a memory of 2 symbols.

Fig. 4.9 depicts the receiver performance for a 2X2 MIMO case where interference is significant. The geometry is similar to the channel for a link with geometry  $\theta_1 = 85^\circ$ ,  $\theta_2 = 85^\circ$ ,  $\phi_1 = 40^\circ$ ,  $\phi_2 = 90^\circ$  and  $d = 20$  m. We call this impulse response  $\mathbf{h}_{11} = 10^{-7} \times (0.0139, 0.1124, 0.0655)$ , which is the same as described in Fig. 4.2. The rest of the geometry is such that  $\mathbf{h}_{12} = \mathbf{h}_{21} = 0.5\mathbf{h}_{11}$  and  $\mathbf{h}_{22} = 2\mathbf{h}_{11}$ . Fig. 4.9 corresponds to the case with a

channel memory of two symbols and so we use the receiver based on the trellis described in Fig. 4.8. It is clearly observable that the MLSE works much better than the optimum MAP detector for both receivers. Interestingly, since the MLSE is based on finding the right sequence of probable inputs to both the transmitters using knowledge of ISI, the MLSE receiver performs much better than the optimum MAP receiver for the high interference case, i.e., channel 1. This means that the MLSE receiver will perform really well even in conditions of high interference and higher noise.

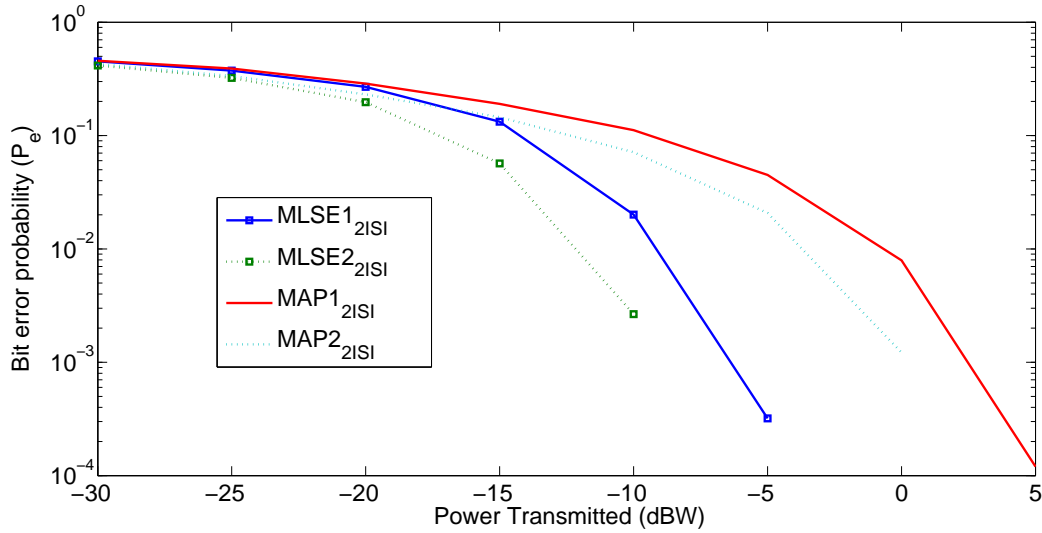


Figure 4.10: Receiver performance comparison for system operating at 3 Mbps and with no interference between channels. The system geometry is  $\theta_1 = 85^\circ$ ,  $\theta_2 = 85^\circ$ ,  $\phi_1 = 40^\circ$ ,  $\phi_2 = 90^\circ$  and  $d = 20$  m for both the transmitter-receiver pairs. Channel with a memory of 2 symbols.

For the geometry described above with no interference between channels, that is, from  $T_x1$  and  $R_x2$ , and vice versa, the MLSE performance remains the same, as shown in Fig. 4.10. The MAP performs significantly better since the interference due to the interfering channel is now zero, leading to less noise at the receiver.

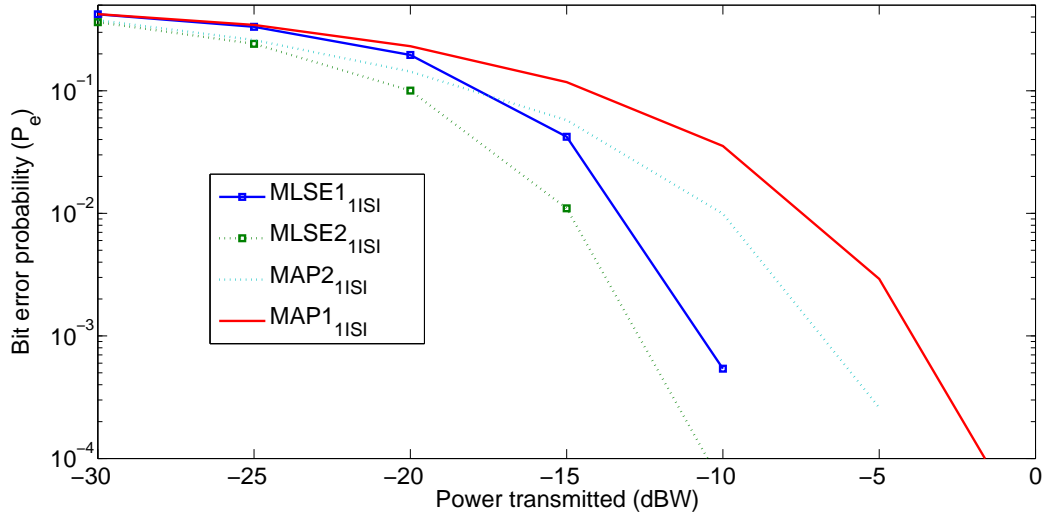


Figure 4.11: Receiver performance comparison for system operating at 2 Mbps and with geometry  $\theta_1 = 85^\circ$ ,  $\theta_2 = 85^\circ$ ,  $\phi_1 = 40^\circ$ ,  $\phi_2 = 90^\circ$  and  $d = 20$  m for both the transmitter-receiver pairs. Channel with a memory of 1 symbol.

When a system with the same geometry as described above is operated at a rate of 2 Mbps, the channel has a memory of one symbol. The receiver performance for the MLSE detector vs. the MAP detector for such a case

is as shown in Fig. 4.11 above. Note that results are identical to those in Fig. 4.10. Again, the MLSE outperforms the MAP detector.

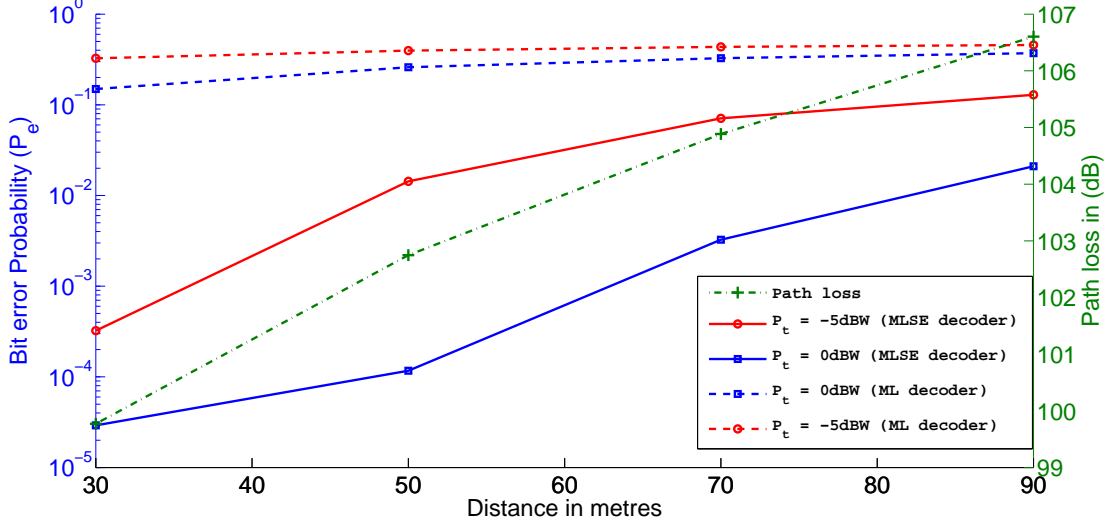


Figure 4.12: MLSE receiver vs. one shot ML receiver (designed for nondispersive channel) performance comparison for system operating at 3 Mbps and with geometry  $\theta_1 = 90^\circ$ ,  $\theta_2 = 90^\circ$ ,  $\phi_1 = 40^\circ$  and  $\phi_2 = 90^\circ$  as distance varies. The solid lines are MLSE BER performance, the dashed lines are the one shot ML decoder BER performance and the dashed line with + marker is the path loss.

Fig. 4.12 compares the performance of the MLSE with the one shot ML receiver described in Chapter 3 for different transmit power levels and increasing distance. For data rates of 3 Mbps and the same geometry ( $\theta_1 = 85^\circ$ ,  $\theta_2 = 85^\circ$ ,  $\phi_1 = 40^\circ$ ,  $\phi_2 = 90^\circ$  and  $d = 20$  m) as in the previous case, ISI is



significant. Thus, we see that the MLSE receiver outperforms the one shot ML receiver significantly. The path loss increases with increasing distance, as shown. Moreover, since the overlapping volume between the transmitter and the receiver beams increases, we see more ISI. Thus, the MLSE performance decreases with increasing the distance between the transmitter and the receiver, which worsens both the path loss and ISI. We observe that increasing the power of the transmitted signal also leads to an improvement in the bit error performance of the receiver. This improvement is significant for the MLSE receiver; however, the one shot ML receiver does not show a lot of improvement with transmit power increase since ISI in this case is significant.

The effects of the  $T_x$  beam angle are presented in Fig. 4.13. The performance is shown to be largely insensitive to  $\phi_1$ . This also agrees with previous research [47]. It does not seem surprising since an NLOS UV link relies on abundant medium scattering. As the transmitter beam width increases, the common volume increases, although the power density decreases.

Fig. 4.14 shows that the receiver performance is very sensitive to  $R_x$  FOV. As  $\phi_2$  increases, more energy is collected, and detection performance improves. However, this detection performance decreases for really large receiver FOVs as the ISI becomes significant. Such a case is observed for the  $\phi_1 = 40^\circ, \theta_1 = 90^\circ, \theta_2 = 90^\circ, d = 30$  m geometry, since the transmitter beam

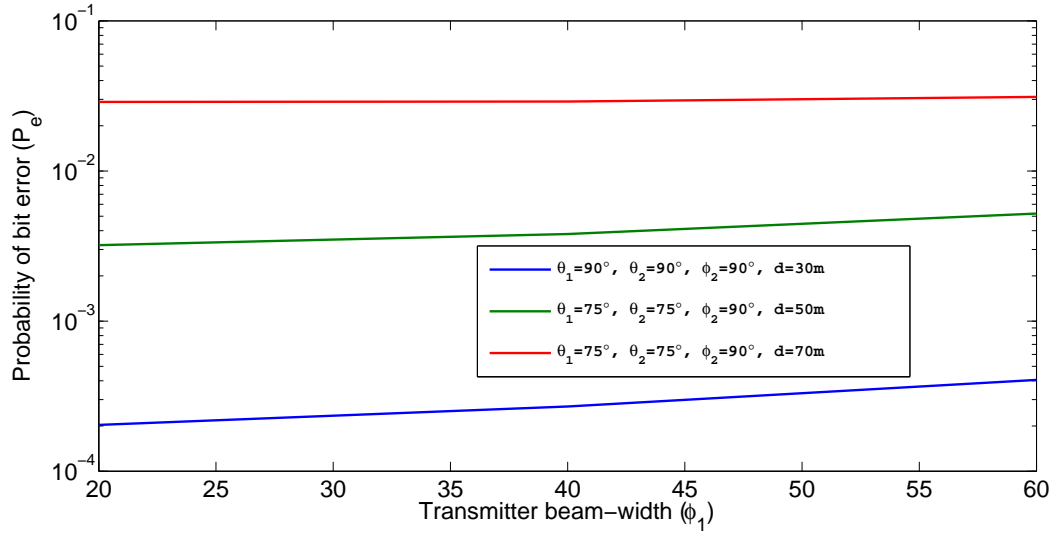


Figure 4.13: MLSE BER performance vs. transmitter beam-width  $\phi_1$  for a system operating at 3 Mbps,  $P_t=-5$  dBW and various geometries.

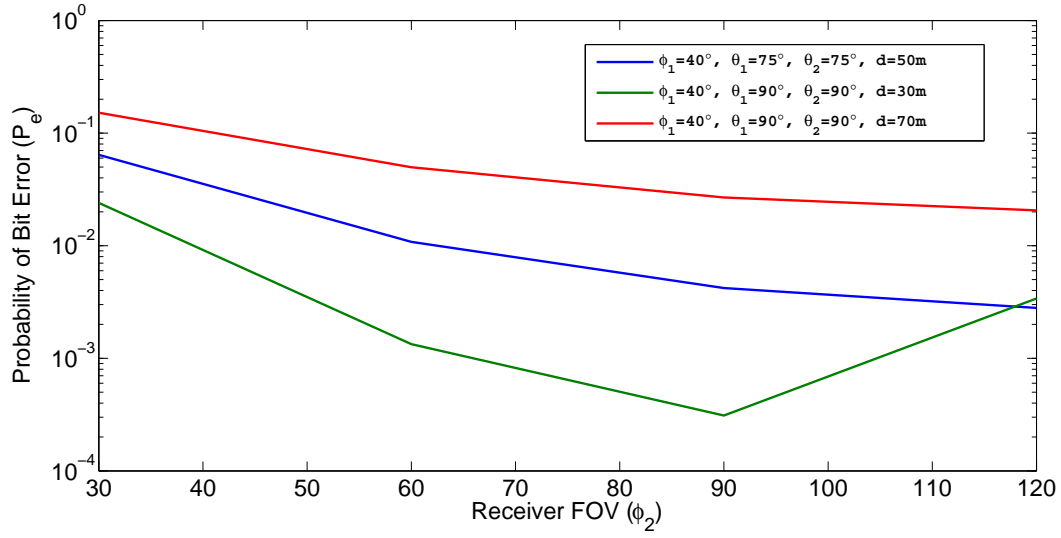


Figure 4.14: MLSE BER performance vs. receiver FOV  $\phi_2$  for a system operating at 3 Mbps,  $P_t=-5$  dBW and various geometries.

and the receiver beams are both pointed vertically up and an increase in the receiver FOV increases ISI significantly. Note that no background radiation is assumed in our study. When background radiation is considered, increasing the receiver FOV can cause significant increase in shot noise.

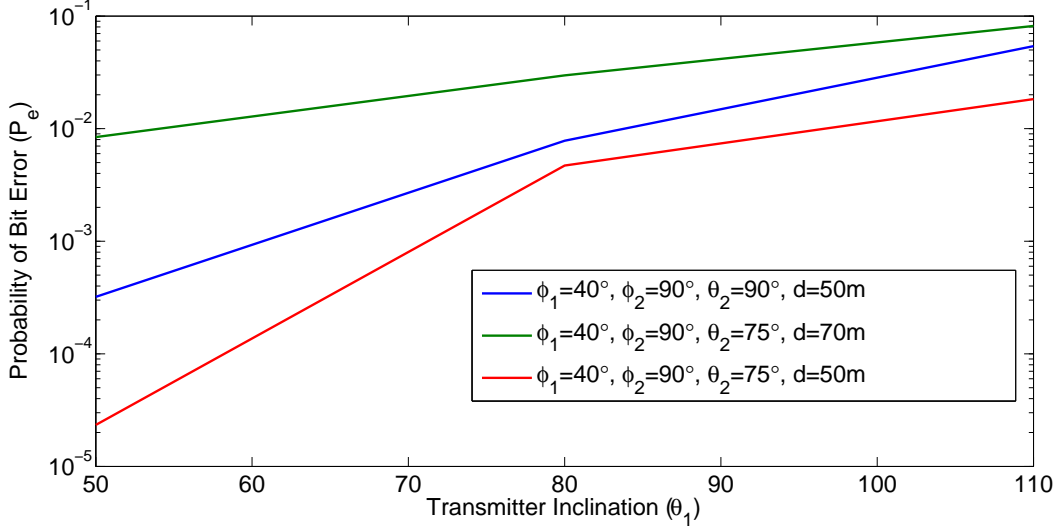


Figure 4.15: MLSE BER performance vs. transmitter inclination  $\theta_1$  for a system operating at 3 Mbps,  $P_t = -5$  dBW and various geometries.

Fig. 4.15 shows the effect of varying the  $T_x$  focal angle. For a large  $\theta_1$ , performance degrades due to a longer propagation path, which results in more loss. The common volume increases only slightly. The effects of  $R_x$  focal angle  $\theta_2$  are demonstrated in Fig. 4.16. Performance is not as sensitive to  $\theta_2$  as it is to  $\theta_1$ . This is because even though the large  $R_x$  FOV increases the common volume as  $\theta_2$  increases, path loss increases much more rapidly

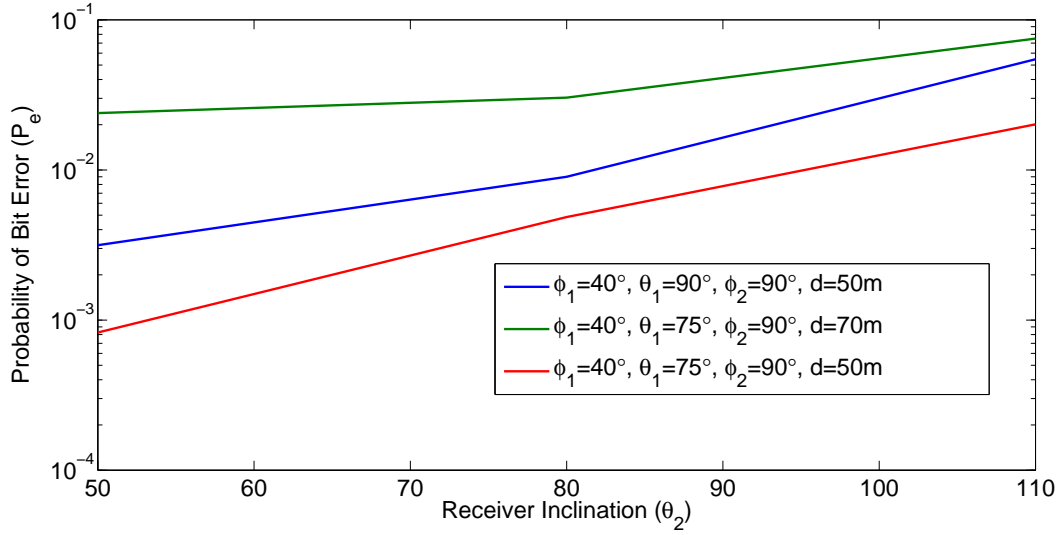


Figure 4.16: MLSE BER performance vs. receiver inclination  $\theta_2$  for a system operating at 3 Mbps,  $P_t=-5$  dBW and various geometries.

due to longer propagation path.

By splitting the transmitter beam and the receiver beam into two narrower beams pointing to the same region and exploiting spatial multiplexing, we observe that the performance of the system using the MLSE receiver is improved even further. This is shown in Fig. 4.18, where, instead of the original transmitter with beam width  $\phi_1^{SISO}$ , the system uses two transmitters with beam widths  $\phi_1^{MIMO} = 10^\circ$ , and at an azimuth difference of  $\phi_1^{SISO} - \phi_1^{MIMO}$  with each other (as shown in Fig. 4.17). Similarly, at the receiver end, two receivers are used, each with field of view  $\phi_2^{MIMO}$  and half the receive area of the original receiver. The original receive for the SISO case has a field

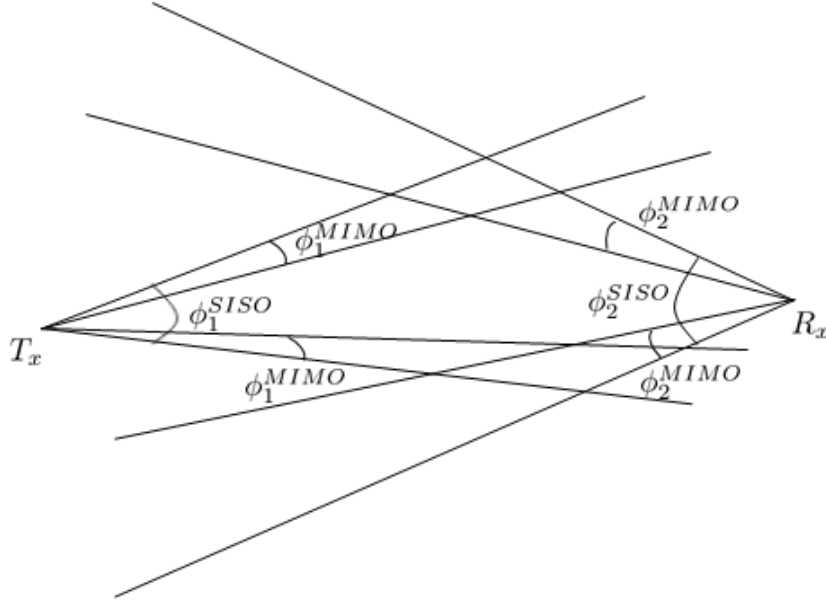


Figure 4.17: Top view of a spatially multiplexed system with two narrower transmit and receive beams instead of a larger beam.

of view  $\phi_2^{SISO}$ . The new transmit-receive pairs operate at half the transmit power and half the data rate of the original SISO pair.

The narrower FOV leads to less receive power but decreases ISI. The ISI effect is also lowered due to the lower data rate on the individual transmitter-receiver pairs in the MIMO system, thereby improving the receiver BER performance. As discussed earlier, the BER performance is almost independent of the transmitter beam width. For the 2X2 case, this BER performance also varies only slightly with the angle between the narrow transmit and receive beams. This makes system design simpler from a practical standpoint, since

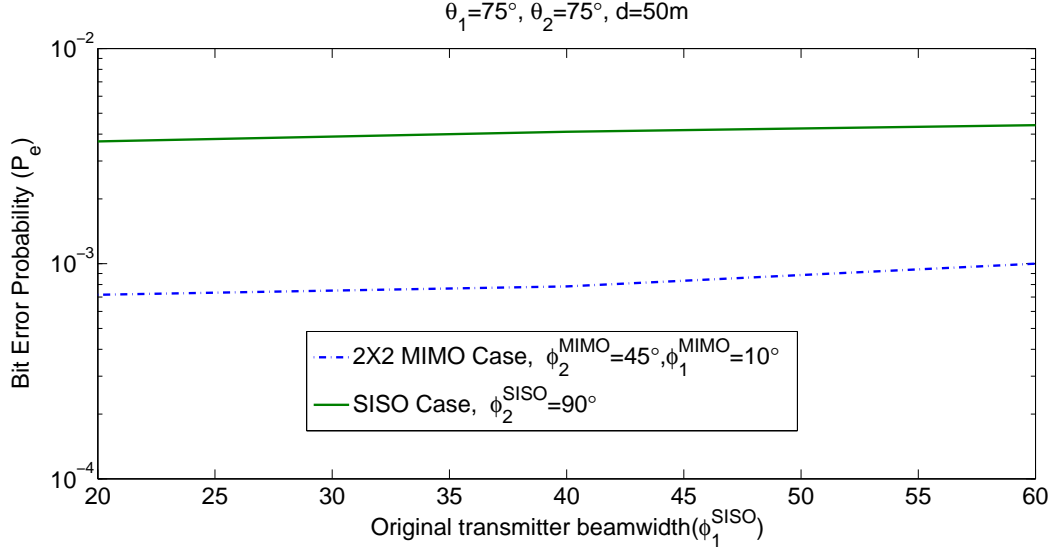


Figure 4.18: MLSE BER performance for the 2X2 spatial multiplexing case vs. the SISO case for different SISO transmitter beam angles/azimuth skew between MIMO narrower transmitters.

the narrow transmit beams do not need to be pointed perfectly towards the receive beams.

Fig. 4.19 shows effects of varying the  $T_x$  focal angle for the spatial multiplexing case. The BER performance of the MLSE receiver for the 2X2 MIMO case surpasses its performance in the SISO case for lower transmitter elevation angles. This is because decreasing the receiver FOV by splitting it into narrower beams and operating them at a lower data rate decreases the ISI for each transmit-receive pair. Moreover, at lower angles, the path loss is lower due to a shorter propagation path and the narrower FOV. At

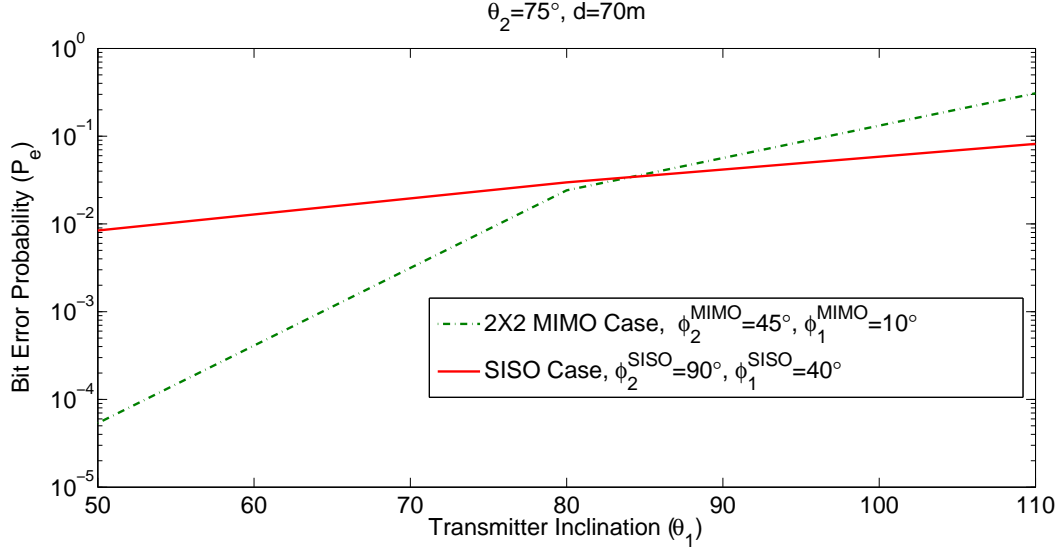


Figure 4.19: MLSE BER performance for the 2X2 spatial multiplexing case vs. the SISO case for different SISO transmitter beam angles/azimuth skew between MIMO narrower transmitters.

higher angles, especially with backscatter angles, the path loss component becomes significant for the transmit power. The MLSE performance for the MIMO case thus degrades slightly when compared to that of the SISO case (the system which operates at twice the power)

## 4.6 Chapter Summary

MLSE is a well-known technique to compensate for pattern-dependent ISI. A sequence detection algorithm for the 2X2 MIMO UV NLOS ISI channel is proposed for two cases, viz., high and low ISI. The BER performance of the

proposed MLSE algorithm is better than the optimum MAP receiver and the one shot ML receiver described in chapter III, but requires higher receiver complexity structure. This is especially true in cases of high data rate and hence, high ISI.

Receiver performance is shown to be independent of transmitter beam width, but depends significantly on the transmitter inclination and the receiver FOV. ISI takes effect for larger receiver FOVs and thus decreases the receiver performance. For lower transmit and receive inclination angles, the path loss is lower and the receiver performs well. Spatial multiplexing improves the BER performance of the MLSE receiver significantly because the narrower FOV and lower data rate on individual links decreases ISI. This performance improvement becomes especially significant for lower transmitter or receiver inclination angles.



# Chapter 5

## Conclusion

This thesis explores multiple aspects of NLOS UV communication systems, including channel modeling, receiver performance evaluation and MIMO systems.

In channel modeling, the research focused on developing ultraviolet path loss models in noncoplanar geometry using the proposed numerical integration approach. This is a new area, because to the best of my knowledge, most work described in existing literature only considers coplanar geometry, which is not applicable for a multiple user scenario. The numerical integration approach reduces the computational complexity and adds additional flexibility for analyzing multibeam cases, i.e., MIMO systems. The proposed approach is compared with a classic single scattering path loss model developed by Reilly et al. and shows a good match in most typical co-planar scenarios.

Using our model we conclude that, pointing requirements for transmit and receive beams can be relaxed by using larger field-of-view receivers or spatial diversity using multiple transmitters/receivers.

This thesis analyzes the performance of the NLOS ultraviolet communication receivers in a nondispersive channel. For low transmit and receive angles and low data rates, inter-symbol interference introduced by channel spread is negligible. Receivers were designed for this nondispersive channel case for the 2X2 MIMO system. Zero forcing, minimum mean square error and the maximum likelihood one shot receivers are presented and their performance for the OOK modulation case is compared to analytically derived results. The results for the receiver performance show the interaction among data rate, bit error rate and transmit/receive geometry.

Due to scattering based propagation and the relatively wide transmission beam angle of commercially available ultraviolet LEDs, inter-symbol interference introduced by channel spread is not negligible. Its effect becomes pronounced at high data rates. However, most of the previous studies ignore the effect of inter-symbol interference. Maximum likelihood sequence estimation receivers were designed for such a case, specifically for the 2X2 MIMO case. Additionally, the one shot maximum a-posteriori probability detector was designed. The MAP receiver makes decisions on a symbol-by-symbol basis, but each symbol decision is based on all possible values of adjacent

signals. The performance of the receivers is analyzed with respect to the connectivity issues of NLOS ultraviolet communication systems in different scenarios, i.e., different transceiver structures, depending on different geometries, power levels and distances. Introducing spatial diversity in the system improves the BER performance of the optimum receiver significantly.

To the best of my knowledge, this research is the first work to study the MIMO NLOS UV communication systems and to take multiple user interference into consideration in the study of connectivity of ultraviolet communication networks.

Future work includes using the models and results from this research to analyze a more complex, fully MIMO case, i.e., a UV NLOS network in settings with shadowing, as well as data rate, distance and system geometry constraints. Furthermore, experiments can be set up to verify the system performance for the MIMO case.

# Bibliography

- [1] G. P. Agrawal. *Fiber-Optic Communication Systems*. Wiley-Interscience, New York, 1992.
- [2] Y.A. Alqudah and M. Kavehrad. MIMO characterization of indoor wireless optical link using a diffuse-transmission configuration. *Communications, IEEE Transactions on*, 51(9):1554 – 1560, Sep 2003.
- [3] X. Bai, D. McIntosh, H. Liu, and J.C. Campbell. Ultraviolet single photon detection with Geiger-mode 4H-SiC avalanche photodiodes. *Photonics Technology Letters, IEEE*, 19(22):1822 –1824, Nov 2007.
- [4] A. Bucholtz. Rayleigh-scattering calculations for the terrestrial atmosphere. *Appl. Opt.*, 34(15):2765–2773, May 1995.
- [5] J.B. Carruther and J.M. Kahn. Angle diversity for nondirected wireless infrared communication. *Communications, IEEE Transactions on*, 48(6):960 –969, Jun 2000.

- [6] S. Chandrasekhar. *Radiative Transfer*. Dover, New York, 1960.
- [7] B. Charles, B. Hughes, E. Andrew, W. Jay, and E. Teppo. An ultraviolet laser based communication system for short range tactical applications. In *Visible and Ultraviolet Lasers and Applications I*, volume 2115 of *Society of Photo-Optical Instrumentation Engineers (SPIE) Conference Series*, pages 79–86, Jan 1994.
- [8] G. Chen, F. Abou-Galala, Z. Xu, and B. M. Sadler. Experimental evaluation of LED-based solar blind NLOS communication links. *Opt. Express*, 16(19):15059–15068, Sep 2008.
- [9] G. Chen, Z. Xu, and B. M. Sadler. Experimental demonstration of ultraviolet pulse broadening in short-range non-line-of-sight communication channels. *Opt. Express*, 18(10):10500–10509, May 2010.
- [10] H. Ding, G. Chen, A. K. Majumdar, and Z. Xu. A parametric single scattering channel model for non-line-of-sight ultraviolet communications. In *Free-Space Laser Communications VIII*, volume 7091 of *Society of Photo-Optical Instrumentation Engineers (SPIE) Conference Series*, August 2008.
- [11] H. Ding, G. Chen, A.K. Majumdar, B.M. Sadler, and Z. Xu. Modeling of non-line-of-sight ultraviolet scattering channels for communication.

- Selected Areas in Communications, IEEE Journal on*, 27(9):1535–1544, December 2009.
- [12] B. Dong, X. Wang, and A. Doucet. A new class of soft MIMO demodulation algorithms. *Signal Processing, IEEE Transactions on*, 51(11):2752–2763, Nov 2003.
- [13] R. J. Drost, T. J. Moore, and B. M. Sadler. UV communications channel modeling incorporating multiple scattering interactions. *J. Opt. Soc. Am. A*, 28(4):686–695, Apr 2011.
- [14] E. S. Fishburne, M. E. Neer, and G. Sandri. Voice communication via scattered ultraviolet radiation. volume 1. Final report, Aeronautical Research Associates of Princeton, Inc, NJ, feb 1976.
- [15] G. Jr. Forney. Maximum-likelihood sequence estimation of digital sequences in the presence of intersymbol interference. *Information Theory, IEEE Transactions on*, 18(3):363–378, May 1972.
- [16] R. M. Gagliardi and S. Karp. *Optical Communications*. John Wiley and Sons, New York, 1976.
- [17] M. Garfield, C. Liang, T. P. Kurzweg, and K. R. Dandekar. MIMO space-time coding for diffuse optical communication. *Microwave and Optical Technology Letters*, 48(6):1108–1110, 2006.

- [18] D. T. Gillespie. Stochastic-analytic approach to the calculation of multiply scattered lidar returns. *J. Opt. Soc. Am. A*, 2(8):1307–1324, Aug 1985.
- [19] Q. He, Z. Xu, and B. M. Sadler. Performance of short-range non-line-of-sight LED-based ultraviolet communication receivers. *Opt. Express*, 18(12):12226–12238, Jun 2010.
- [20] S. Hranilovic and F.R. Kschischang. A pixelated MIMO wireless optical communication system. *Selected Topics in Quantum Electronics, IEEE Journal of*, 12(4):859 –874, July-Aug 2006.
- [21] S. Jivkova, B.A. Hristov, and M. Kavehrad. Power-efficient multispot-diffuse multiple-input-multiple-output approach to broad-band optical wireless communications. *Vehicular Technology, IEEE Transactions on*, 53(3):882 – 889, May 2004.
- [22] J.M. Kahn and J.R. Barry. Wireless infrared communications. *Proceedings of the IEEE*, 85(2):265 –298, Feb 1997.
- [23] S. Karp, R. M. Gagliardi, S. E. Moran, and L. B. Stotts. *Optical Channels: Fibers, Clouds, Water, and the Atmosphere*. Plenum Press, New York, 1988.

- [24] D. Kedar. Multiaccess interference in a non-line-of-sight ultraviolet optical wireless sensor network. *Appl. Opt.*, 46(23):5895–5901, Aug 2007.
- [25] J.R. Kerr, P.J. Titterton, A.R. Kraemer, and C.R. Cooke. Atmospheric optical communications systems. *Proceedings of the IEEE*, 58(10):1691 – 1709, Oct 1970.
- [26] Y. Li and Z. Xu. Wlcp1-09: Transmitted reference schemes for wireless optical communications. In *Global Telecommunications Conference, 2006. GLOBECOM '06. IEEE*, pages 1 –5, 27 2006-dec. 1 2006.
- [27] M. R. Luetttgen, J. H. Shapiro, and D. M. Reilly. Non-line-of-sight single-scatter propagation model. *J. Opt. Soc. Am. A*, 8(12):1964–1972, Dec 1991.
- [28] R. Mesleh, H. Elgala, and H. Haas. Optical spatial modulation. *J. Opt. Commun. Netw.*, 3(3):234–244, Mar 2011.
- [29] D. C. O’Brien. Indoor optical wireless communications: recent developments and future challenges. In *Free-Space Laser Communications IX*, volume 7464 of *Society of Photo-Optical Instrumentation Engineers (SPIE) Conference Series*, pages 74640B–74640B–12, 2009.
- [30] J.J. Puschell and R. Bayse. High data rate ultraviolet communication systems for the tactical battlefield. In *Tactical Communications Confer-*



- ence, 1990. Vol.1. *Tactical Communications. Challenges of the 1990's, Proceedings of the*, pages 253 –267, Apr 1990.
- [31] M. Razavi and J.H. Shapiro. Wireless optical communications via diversity reception and optical preamplification. *Wireless Communications, IEEE Transactions on*, 4(3):975 – 983, May 2005.
- [32] D. M. Reilly. Atmospheric optical communications in the middle ultraviolet. Master's thesis, MIT, Cambridge, MA, 1976.
- [33] D. M. Reilly, D. T. Moriarty, and J. A. Maynard. Unique properties of solar blind ultraviolet communication systems for unattended ground sensor networks. In E. M. Carapezza, editor, *Unmanned/Unattended Sensors and Sensor Networks*, volume 5611 of *Society of Photo-Optical Instrumentation Engineers (SPIE) Conference Series*, pages 244–254, November 2004.
- [34] M.L.B. Riediger, R. Schober, and L. Lampe. Blind detection of on-off keying for free-space optical communications. In *Electrical and Computer Engineering, 2008. CCECE 2008. Canadian Conference on*, pages 001361 –001364, May 2008.
- [35] S. A. Self. Focusing of spherical Gaussian beams. *Appl. Opt.*, 22(5):658–661, Mar 1983.

- [36] M. Shatalov, J. Zhang, A.S. Chitnis, V. Adivarahan, J. Yang, G. Simin, and M.A. Khan. Deep ultraviolet light-emitting diodes using quaternary AlInGa<sub>N</sub> multiple quantum wells. *Selected Topics in Quantum Electronics, IEEE Journal of*, 8(2):302–309, Mar/Apr 2002.
- [37] G. Shaw, A. Seigel, and J. Model. Ultraviolet comm links for distributed sensor systems. *IEEE LEOS Magazine*, 19(5):26–29, 2005.
- [38] G. A. Shaw and M. Nischan. Short-range NLOS ultraviolet communication testbed and measurements. In *Battlespace Digitization and Network-Centric Warfare*, volume 4396 of *Society of Photo-Optical Instrumentation Engineers (SPIE) Conference Series*, pages 31–40, Aug 2001.
- [39] G. A. Shaw, A. M. Siegel, and J. Model. Extending the range and performance of nonline-of-sight ultraviolet communication links. In *Unattended Ground, Sea, and Air Sensor Technologies and Applications VIII*, volume 62310C of *Society of Photo-Optical Instrumentation Engineers (SPIE) Conference Series*, pages 1–12, Apr 2006.
- [40] G. A. Shaw, A. M. Siegel, and M. L. Nischan. Demonstration system and applications for compact wireless ultraviolet communications. In *Sensors, and Command, Control, Communications, and Intelligence*

- (C3I) *Technologies for Homeland Defense and Law Enforcement II*, volume 5071 of *Society of Photo-Optical Instrumentation Engineers (SPIE) Conference Series*, pages 241–252, Sep 2003.
- [41] L. B. Stotts and D. D. Bryski. Unattended ground sensor related technologies: an army perspective. In *Unattended Ground Sensor Technologies and Applications IV*, volume 4743 of *Society of Photo-Optical Instrumentation Engineers (SPIE) Conference Series*, pages 1–9, Aug 2002.
- [42] D. E. Sunstein. *A Scatter Communications Link at Ultraviolet Frequencies*. PhD thesis, MIT, Cambridge, MA, 1968.
- [43] D. Takase and T. Ohtsuki. Spatial multiplexing in optical wireless MIMO communications over indoor environment. *IEICE Trans Commun*, E89-B(4):1364–1370, 2006.
- [44] L. Wang, Q. He, Z. Xu, and B. M. Sadler. Performance of non-line-of-sight ultraviolet communication receiver in ISI channel. In *Free Space Laser Communications IX*, volume 1-3 of *Society of Photo-Optical Instrumentation Engineers (SPIE) Conference Series*, Aug 2010.
- [45] L. Wang, Z. Xu, and B. M. Sadler. An approximate closed-form link loss model for non-line-of-sight ultraviolet communication in noncoplanar

- geometry. *Opt. Lett.*, 36(7):1224–1226, Apr 2011.
- [46] R. Xu and F.C.M. Lau. Performance analysis for MIMO systems using zero forcing detector over fading channels. *Communications, IEEE Proceedings-*, 153(1):74 – 80, Feb 2006.
- [47] Z. Xu. Approximate performance analysis of wireless ultraviolet links. In *Acoustics, Speech and Signal Processing, 2007. ICASSP 2007. IEEE International Conference on*, volume 3, pages III–577 –III–580, Apr 2007.
- [48] Z. Xu, H. Ding, B. M. Sadler, and G. Chen. Analytical performance study of solar blind non-line-of-sight ultraviolet short-range communication links. *Opt. Lett.*, 33(16):1860–1862, Aug 2008.
- [49] Z. Xu and B.M. Sadler. Ultraviolet communications: Potential and State-Of-The-Art. *Communications Magazine, IEEE*, 46(5):67–73, May 2008.
- [50] A. S. Zachor. Aureole radiance field about a source in a scattering-absorbing medium. *Appl. Opt.*, 17(12):1911–1922, Jun 1978.
- [51] Hailiang Zhang, Hongwei Yin, Honghui Jia, Juncai Yang, and Shengli Chang. Study of effects of obstacle on non-line-of-sight ultraviolet communication links. *Opt. Express*, 19(22):21216–21226, Oct 2011.